Scientific Research Publishing

Journal of Applied Mathematics and Physics, 2026, 14(2), 523-558
https://www.scirp.org/journal/jamp
ISSN Online: 2327-4379
ISSN Print: 2327-4352

Emergent Golden Ratio Geometries in the Simulated Unified Resultant Amplitude Method: Bridging Wave Superpositions to Cuboctahedral Symmetries in Unified Physics

Shawn P. Guillory

Department of Mechanical Engineering, The University of Louisiana at Lafayette, Lafayette, USA
Email: secured_email_cae@proton.me

How to cite this paper: Guillory, S.P. (2026) Emergent Golden Ratio Geometries in the Simulated Unified Resultant Amplitude Method: Bridging Wave Superpositions to Cuboctahedral Symmetries in Unified Physics. *Journal of Applied Mathematics and Physics*, **14**, 523-558.
https://doi.org/10.4236/jamp.2026.142028

Received: December 23, 2025
Accepted: January 30, 2026
Published: February 2, 2026

Abstract

This study presents a conceptual and geometrically motivated exploration of structured wave superposition using the Simulated Unified Resultant Amplitude Method (S-URAM), with particular emphasis on emergent hexagonal structures and their relation to the cuboctahedron in contemporary unification efforts. Through the application of radial wave overlays, critical intersection points produce configurations whose proportions naturally conform to the golden ratio (φ). Symmetric reflection of these patterns exhibit fractal-like scaling behavior comparable to the second iteration of the Koch snowflake, indicating inherent recursive self-similarity. Extending to three-dimensional cuboctahedral symmetry, phenomenological expressions are developed for the inverse fine-structure constant, the weak mixing angle, and the strong coupling constant—interpreting parameters and their refinements as arising from golden-ratio phase constraints, chiral asymmetries, volumetric corrections, and edge-multiplicity scaling. These results suggest a direct geometric linkage between S-URAM wave dynamics, polyhedral symmetry, and central concepts in unified physics—including Einstein field equations, grand unified theories, and quantum gravity & holographic mass frameworks. While the present work does not claim a replacement for established theories, by highlighting scalable, self-similar geometries that echo natural constants and structures, this approach offers fresh conceptual insights into bridging quantum mechanics, general relativity, and fractal descriptions of spacetime.

Keywords

Waves, Golden Ratio, Fractals, Polyhedral, Unified Theory, Fine-Structure Constant

1. Introduction

The quest for a unified theory reconciling quantum mechanics with general relativity remains one of the greatest challenges in theoretical physics [1]-[5]. While significant progress has been made in unifying fundamental forces, a seamless framework integrating the quantum realm with the macroscopic curvature of spacetime remains elusive. Geometrical approaches offer promising pathways forward, with specific symmetries and polyhedral structures providing fresh insights into the fabric of reality [6]-[11].

Geometry has long been foundational to physics, from the Euclidean constructions underlying classical mechanics to non-Euclidean differential geometry central to Einstein's Field Equations (EFE) [12]-[14]. Schwarzschild's solution to Einstein's Field Equations exemplifies this geometric essence [15]-[17]. However, unifying quantum mechanics with general relativity remains active alongside attempts to understand the origin of physical constants, the scaling of natural structures, and the possible discrete or self-organizing nature of spacetime [13]-[20].

Among the many proposed geometric frameworks, polyhedral symmetries, including those of the cuboctahedron and fractal relationships thereof, have emerged as interesting avenues toward unification. Haramein and Rauscher demonstrated that this structure naturally arises in modified forms of Einstein's Field Equations (EFE) and Grand Unified Theories (GUTs) through the incorporation of torque and Coriolis force effects [6]. In connection with Quantum Gravity & Holographic Mass (QGHM) frameworks, it represents the dense tangent packing of Planck Spherical Units (PSU), potentially bridging gravity with the strong nuclear force [16]-[20].

Complementing these ideas, the golden ratio ($\varphi \approx 1.618$) has continued to attract attention for its presence in self-similar patterns, biological growth processes, and fractal structures, evident in phenomena ranging from phyllotaxis (the arrangement of leaves on a stem) to galactic spirals [21]-[31]. Building on this mathematical ubiquity, various authors have proposed that φ may play a more fundamental role in physical systems, potentially relating to harmonic structures, hierarchical scaling, and geometric symmetries [26]-[28] [32]-[34]. Parallel to this, the fine-structure constant ($\alpha \approx 1/137$), long viewed as one of the most enigmatic quantities in physics, represents another focal point in this geometric discourse. While α emerges naturally within quantum electrodynamics (QED), its mathematical origin and apparent fine-tuning remain unclear [35]. Some researchers—particularly those working with fractal geometries, golden-ratio scaling, or quasi-

Euclidean models—have sought to relate α to geometric invariants or self-similar relationships [36]-[45]. Although no consensus has been reached, these efforts exemplify a broader interest in connecting dimensionless constants to underlying geometric structures and examining whether self-similar geometry and golden-ratio relationships could be indicative of deeper symmetries within the laws of physics.

Within this conceptual landscape, the present study investigates the Simulated Unified Resultant Amplitude Method (S-URAM), a recently developed geometric framework that models multi-dimensional superposition through simulated wave-summation patterns with having demonstrated practical validity in kinematics and differential equation applications [46]. In cam theory and associated design, S-URAM's resultant amplitude method simulates the superposition of angular displacements and velocities, enabling precise prediction of follower motion profiles under opposing harmonic forces—validating its utility in mechanical systems engineering and lending empirical weight to its geometric extensions in unified physics. Rooted in Euler's formula and frequency-based constructive/destructive interference, S-URAM produces emergent geometric structures exhibiting symmetry, oscillatory regularity, and fractal-like features. In connection and consistent with Fourier's theorem and modern quantum theory, all of spacetime can be mathematically modeled as modes of oscillation. Consequently, S-URAM in context of Fourier analysis stands at the heart of quantum mechanics—which should be able to be reasonably extrapolated and extended to unified mathematical/physics-based representations of such [47] [48].

Moreover, this work explores how S-URAM geometries relate to the cuboctahedron—particularly through its 2D hexagonal projections—and whether golden-ratio relationships arise naturally from these constructions. It highlights several geometric constructs—such as ellipses, Euclidean triangles, and circular overlays—that appear both within S-URAM and in diverse physical contexts ranging from orbital mechanics to group-theoretic formulations of field equations [49]-[55]. These additional connections suggest that S-URAM's geometric outputs may intersect with multiple strands of theoretical physics, even if only at a conceptual level. The central objective is not to assert a definitive physical model but to examine whether this geometric structure may provide conceptual insight into unique patterns potentially relevant to quantum-scale behavior, classical gravitational structure, or scaling laws observed across nature. This includes deriving an approximate expression for the inverse fine-structure constant from 2D S-URAM constraints (**Appendix C**), with a 3D extension yielding exceptional precision for α^{-1} (matching CODATA to ~10^{-10} relative error; **Appendix D**), a further extension approximating the weak mixing angle $\sin^2\theta_W$ from phase deviations and PSU packing (**Appendix E**), and an additional derivation for the strong coupling constant $\alpha_s(M_Z)$ from gluon-edge multiplicity and recursive corrections (**Appendix F**), interpreting α, θ_W, and α_s as geometric rotational coupling, mixing ratios, and binding strengths from golden-ratio phase constraints and volumetric corrections in

cuboctahedral symmetry [56].

Fractal geometry provides additional motivation for this analysis. Since Mandelbrot's work on self-similarity [23], fractals have been applied to phenomena across physics, from cosmological clustering to irregularities within quantum systems [57]-[59]. If the universe exhibits fractal-like behavior across different scales, then geometric frameworks capable of producing self-similar or recursively structured patterns—such as S-URAM-cuboctahedral-golden ratio connected geometries—may offer a conceptual bridge between scale-dependent descriptions of physical law. This does not imply that spacetime is necessarily fractal in a strict mathematical sense, but rather that fractal-inspired analyses may reveal structural parallels or scaling behaviors of theoretical interest [57]-[61].

Overall, this work aims to contribute a mathematically grounded, geometrically motivated preliminary framework and analysis of S-URAM constructions and their potential relevance to ongoing discussions surrounding polyhedral symmetry, scaling laws, and geometric interpretations of fundamental constants. Rather than proposing a complete unified theory, the study seeks to illuminate how specific geometric patterns—particularly those comprising the cuboctahedron, hexagonal projections, and the golden ratio in connection with Einstein's Field Equations, Grand Unified Theories, and Quantum Gravity & Holographic Mass frameworks—may provide avenues for future research into the deeper structure of physical law.

Scope and Limitations: The results presented in this work are intended as a geometrically motivated and phenomenological framework rather than serving as a complete derivation of physical constants from first principles of quantum field theory or the Standard Model. While numerical correspondences with known physical parameters are explored and shown to arise naturally from the imposed geometric constraints, no claim is made that the Simulated Unified Resultant Amplitude Method (S-URAM) replaces or supersedes established gauge-theoretic or renormalization-based formulations. Instead, the constructions and exploratory extensions presented herein are offered as conceptual insights into possible geometric structures and scaling relationships that may underlie, approximate, or complement existing physical theories. Further mathematical development and independent physical validation would be required to establish any deeper theoretical or empirical significance. Nevertheless, and for those interested in a field-theoretic perspective, an illustrative Lagrangian linking S-URAM geometric constraints to effective couplings is provided in Section 3.2.

In connection, while the derivations in **Appendices C-F** are phenomenological and do not claim causal derivation from first principles, they distinguish numerical coincidence from potential structural parallels through a shared geometric mechanism: S-URAM's wave superposition constraints (e.g., radial overlays enforcing φ-embedded phase $\varnothing = \tan^{-1}\varphi$) generate emergent asymmetries in cuboctahedral projections, interpreted as rotational couplings (for α), chiral devia-

tions (for θ_W), and edge-multiplicity bindings (for α_s). This echoes torque/Coriolis-induced symmetries in modified Einstein field equations [6] [16]-[20], suggesting a unified conceptual motif where spacetime granularity (PSU packing) imprints constants via self-similar scaling, rather than ad-hoc fitting. Causal validation would require embedding in full Quantum Field Theory (QFT) simulations.

2. Methods

2.1. Geometric Structures that Arise from S-URAM Geometry—Ellipses, Euclid Triangles & Critical Points of Intersection (State 1)

S-URAM geometry encompasses intricate structures such as ellipses, Euclid triangles (right-angled triangles as described in Euclidean geometry), and critical points of intersection. These elements are essential for the mathematical constraints that lead to golden ratio relationships throughout the system. While 2D S-URAM waves span four Cartesian quadrants, we focus here only on the first quadrant and then reflect the geometry into the other quadrants (in Section 2.6) to achieve a symmetric configuration that can be scaled recursively to form an infinite number of multiplicities. Figure 1 illustrates the geometry used throughout this section.

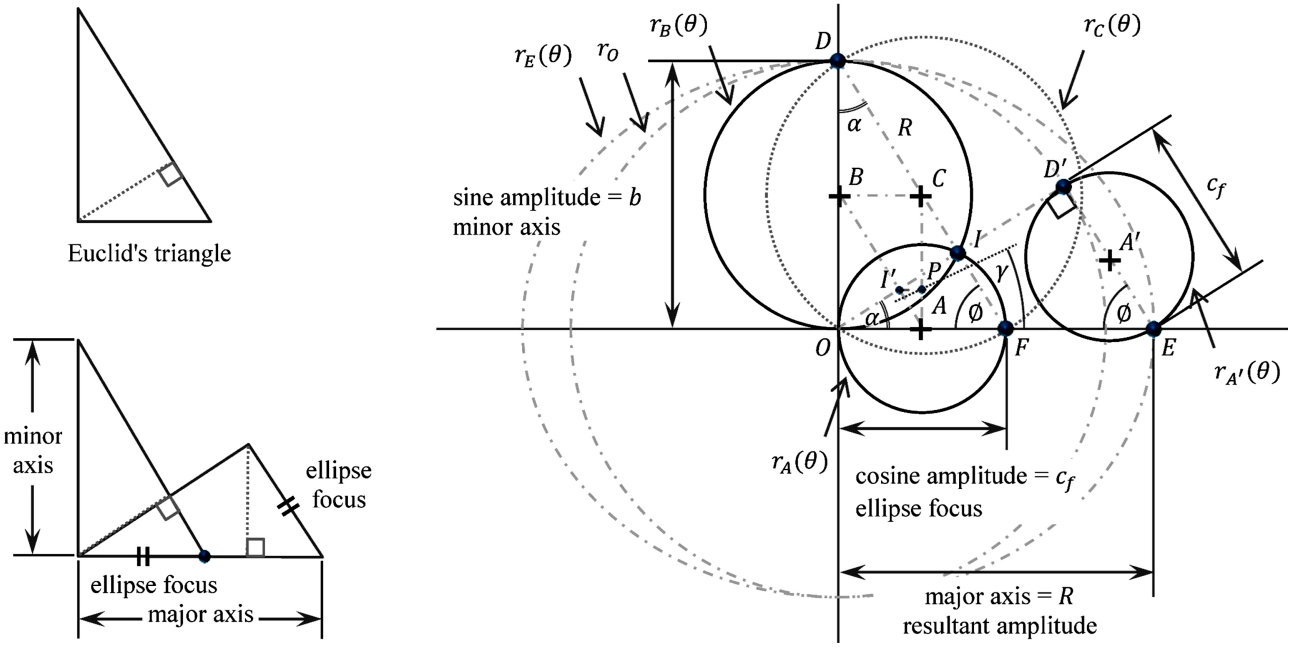

Figure 1. Geometric structures of polar waves (ellipses, Euclid triangles & critical points).

Radial Sine Wave and Parametric Form

Let point O represent the origin of the 2D Cartesian plane. Essential to the geometric formulation, we first define a radial sine wave $r_B(\theta)$ about point B, mathematically described by the polar/parametric Equations (1) through (3). Here, the sine amplitude axis b (a specified quantity) spans line $\overline{OD} = b$, and the half-distances are $\overline{OB} = \overline{BD} = b/2$.

$$r_B(\theta) = b\sin\theta \tag{1}$$

$$x_B(\theta) = r_B(\theta)\cos\theta = (b\sin\theta)\cos\theta = \frac{b}{2}\sin(2\theta) \tag{2}$$

$$y_B(\theta) = r_B(\theta)\sin\theta = (b\sin\theta)\sin\theta = b\sin^2\theta \tag{3}$$

We rotate this sine amplitude axis about the origin O, resulting in a centered circle r_O, described by the polar/parametric Equations (4) through (6):

$$r_O = b, \tag{4}$$

$$x_O(\theta) = r_O\cos\theta = b\cos\theta, \tag{5}$$

$$y_O(\theta) = r_O\sin\theta = b\sin\theta. \tag{6}$$

Point D' on the centered circle r_O is defined at an arbitrary angle from the horizon (within the first quadrant) to form a radial line $\overline{OD'} = b$. Its orthonormal line $\overline{D'E}$ intersects the abscissa at point E, defining the major axis $\overline{OE}$ of the ellipse—a curve that arises in Kepler's laws of planetary motion and central-force dynamics among others [49]-[52]. This also defines $\overline{OD}$ as the minor axis and $\overline{D'E}$ as the ellipse's focus distance c_f, the distance from the origin O to the elliptical focus point A. The equation of this ellipse, $r_E(\theta)$, is expressed in polar/parametric form by Equations (7) through (9):

$$x_E(\theta) = c_f\cos\theta, \tag{7}$$

$$y_E(\theta) = b\sin\theta, \tag{8}$$

$$r_E(\theta) = \sqrt{x_E(\theta)^2 + y_E(\theta)^2} = \sqrt{c_f^2\cos^2\theta + b^2\sin^2\theta}. \tag{9}$$

Radial Cosine Wave and Parametric Form

The fundamental geometric property $\overline{D'E} = c_f$ holds for any arbitrary location of D' within the first quadrant, allowing the construction of a circle $r_{A'}(\theta)$ about the midpoint (denoted as A') of $\overline{D'E}$. This circle is then translated to point O, creating a non-shifted radial cosine wave about point A. The polar/parametric equations for this wave $r_A(\theta)$ are given by Equations (10) through (12), where $a = c_f$ is the amplitude axis and the half-distances are $\overline{OA} = \overline{AF} = \overline{D'A'} = \overline{A'E} = c_f/2$. The inclusion of corresponding radial sine and cosine waves connects with S-URAM theory [46].

$$r_A(\theta) = c_f\cos\theta \tag{10}$$

$$x_A(\theta) = r_A(\theta)\cos\theta = (c_f\cos\theta)\cos\theta = c_f\cos^2\theta \tag{11}$$

$$y_A(\theta) = r_A(\theta)\sin\theta = (c_f\cos\theta)\sin\theta = \frac{c_f}{2}\sin(2\theta) \tag{12}$$

Note that we consider c_f as a specified quantity, allowing direct specification of both S-URAM waves—the radial sine and cosine wave amplitudes (b and $a = c_f$, respectively). The "arbitrary" angle of $\overline{OD'}$ from the horizon now depends on these values, resulting in the system (**Figure 1**) having *two degrees of geometric freedom*.

S-URAM Triangle and Wave Parameters

From the amplitude axes $a = c_f$ and b, the S-URAM triangle ΔODF is formed [46] congruent to $\Delta OD'E$, revealing the resultant amplitude R, phase angle $\varnothing$ and its opposite angle α. These parameters are defined by Equations (13) through (17):

$$R = \overline{DF} = \overline{OE} = \sqrt{c_f^2 + b^2}, \tag{13}$$

$$\varnothing = \tan^{-1}\left|\frac{b}{c_f}\right|, \tag{14}$$

$$\alpha = \frac{\pi}{2} - \varnothing, \tag{15}$$

$$\cos\varnothing = \sin\alpha = \frac{c_f}{R}, \tag{16}$$

$$\sin\varnothing = \cos\alpha = \frac{b}{R}. \tag{17}$$

Given these parameters, the circle $r_A(\theta)$ is expressed in polar/parametric form by Equations (18) through (22):

$$h = \overline{OD'}\cos\alpha - \overline{OA} + \overline{D'A'}\cos\varnothing = \frac{b^2}{R} - \frac{c_f}{2} + \frac{c_f^2}{2R} \tag{18}$$

$$k = \overline{A'E}\sin\varnothing = \frac{bc_f}{2R} \tag{19}$$

$$x_{A'}(\theta) = x_A(\theta) + h = c_f\cos^2\theta + h \tag{20}$$

$$y_{A'}(\theta) = y_A(\theta) + k = \frac{c_f}{2}\sin(2\theta) + k \tag{21}$$

$$r_{A'}(\theta) = \sqrt{x_{A'}(\theta)^2 + y_{A'}(\theta)^2} \tag{22}$$

Resultant Wave and Geometric Parameters

The sine and cosine waves $r_B(\theta)$ and $r_A(\theta)$, as well as line $\overline{OD'}$, intersect at point I. Their summation produces the resultant wave $r_C(\theta)$, centered at point C (midpoint of $DF = R$). The algebraic sign augmentations of R and $\varnothing$ (from S-URAM equations [46]) fluctuate with the quadrant position of the triangle formed by the sine and cosine amplitudes, as defined by Equations (23) and (24). We evaluate at quadrant one ($q = 1$) for simplicity.

$$\hat{R} = \prod_{m=1}^{q} \mathrm{e}^{\mathrm{i}(m-1)\pi} = (-1)^{\mathrm{Floor}\left(\frac{q}{2}\right)} = \frac{a}{|a|} \Rightarrow (+1) \tag{23}$$

$$\hat{\varnothing} = -\mathrm{e}^{\mathrm{i}(q-1)\pi} = -\cos\pi(q-1) - \mathrm{i}\sin\pi(q-1) = -\frac{ab}{|ab|} \Rightarrow (-1) \tag{24}$$

$$r_C(\theta) = \hat{R}R\cos\left(\theta + \hat{\varnothing}\varnothing\right) = R\cos(\theta - \varnothing) \tag{25}$$

$$x_C(\theta) = r_C(\theta)\cos\theta = R\cos(\theta - \varnothing)\cos\theta \tag{26}$$

$$y_C(\theta) = r_C(\theta)\sin\theta = R\cos(\theta - \varnothing)\sin\theta \tag{27}$$

Intricate Geometric Characteristics

From the intersection of S-URAM waves at point I, we generate $\overline{OI}$, orthonormal to $\overline{DF}$, forming Euclid triangle ΔODF. S-URAM wave points A, B, and C lead to additional Euclid triangles ΔOAB and ΔCAB, similar to and proportionally smaller than ΔODF. Interesting to note, Euclid triangles appear in some unified theory attempts [53] [54]. Nevertheless, and continuing, orthonormal lines $\overline{AB}$ and $\overline{OI}$ intersect at point I. A horizontal line from I' intersects $\overline{AC}$ at point P, forming $\Delta API'$. Points P and I are crucial for mathematical constraints. Furthermore, an isosceles triangle ΔOPF arises due to congruence between $\overline{OP}$ and $\overline{PF}$. Relevant distances and angle γ (from abscissa to $\overline{OP}$) are defined by Equations (28) through (34):

$$\overline{OI} = r_B(\alpha) = r_A(\alpha) = \frac{bc_f}{R}, \tag{28}$$

$$\overline{BA} = \overline{DC} = \overline{CF} = \frac{R}{2}, \tag{29}$$

$$\overline{OI'} = \frac{1}{2}\overline{OI} = \frac{bc_f}{2R}, \tag{30}$$

$$\overline{I'P} = \overline{OA} - \overline{OI'}\cos\alpha = \frac{c_f}{2} - \frac{c_f b^2}{2R^2} = \frac{c_f}{2}\left(1 - \frac{b^2}{R^2}\right), \tag{31}$$

$$\overline{AP} = \overline{OI'}\sin\alpha = \frac{bc_f^2}{2R^2}, \tag{32}$$

$$\overline{OP} = \overline{PF} = \sqrt{\overline{OA}^2 + \overline{AP}^2} = \sqrt{\left(\frac{c_f}{2}\right)^2 + \left(\frac{bc_f^2}{2R^2}\right)^2} = \frac{c_f}{2}\sqrt{1 + \frac{bc_f}{R^2}}, \tag{33}$$

$$\gamma = \tan^{-1}\frac{\overline{AP}}{\overline{OA}} = \tan^{-1}\left(\frac{\left(bc_f^2\right)/\left(2R^2\right)}{\left(c_f/2\right)}\right) = \tan^{-1}\left(\frac{bc_f}{R^2}\right). \tag{34}$$

At this stage, all geometric structures are defined within State 1, yielding a 2D S-URAM system (**Figure 1**) with *two degrees of geometric freedom* due to numerical independence between sine and cosine amplitudes. This forms the foundation for subsequent constraints.

2.2. Radial Cosine Wave Overlay & Mathematical Constraints (State 2)

In this section, we introduce a radial cosine wave overlay and examine how constraining it to points P and I modifies the S-URAM geometry. The derivation for State 2 is divided into four phases: (1) free overlay, (2) overlay constrained to pass through point P, (3) overlay constrained to pass through point I, and (4) overlay constrained to pass through both points P and I simultaneously. **Figure 2** illustrates the geometry in Phases 1-4.

This overlay bears similarity to a quantum couple, as seen in research approximating the fine-structure constant using Planck cubes, spheres, uncertain bound-

aries, UV/IR half-wavelength cutoffs, and symmetries across multi-dimensional spaces [55]. Consequently, this may offer a pathway to new geometrical formulations embedding the golden ratio.

Phase 1: Free Overlay

We duplicate circle $r_A(\theta)$ and translate it to point A'' by arbitrary distance $\overline{OO'}$ along the abscissa, creating the radial cosine wave overlay $r_{A''}(\theta)$, confined between O' and F', as described by Equations (35) through (36):

$$x_{A''}(\theta) = x_A(\theta) + \overline{OO'} = c_f \cos^2\theta + \overline{OO'}, \tag{35}$$

$$y_{A''}(\theta) = y_A(\theta) = \frac{c_f}{2}\sin(2\theta), \tag{36}$$

The circles intersect at I'', with J as the overlay center. Point P' is horizontally aligned with P. $\overline{O'F'}$ is the cosine amplitude c_f, and $\overline{O'A''} = \overline{A''F'}$ is its half-distance:

$$\overline{OA''} = \overline{OO'} + \overline{O'A''} = \overline{OO'} + (c_f/2), \tag{37}$$

$$\overline{OF'} = \overline{OA''} + \overline{A''F'} = \overline{OO'} + c_f, \tag{38}$$

$$\overline{OJ} = \overline{OF'}/2 = \left(\overline{OO'} + c_f\right)\Big/2. \tag{39}$$

The geometry now has *three degrees of geometric freedom*, where b, c_f, and $\overline{OO'}$ are independent, specified quantities.

Phase 2: Constrained to Point *P*

The circle $r_A(\theta)$ is constrained so P and P' coincide, limiting $\overline{OO'}$ as a function of b and c_f, reducing to *two degrees of geometric freedom*. We impose $\overline{PP'} = 0$ ($\overline{OP} = \overline{OP'}$), resolving into vertical and horizontal constraints. Equation (40) solves for β (angle of $\overline{O'P''}$ from abscissa) in Equation (41); Equation (42) solves for $\left(\overline{OO'}\right)_1$ in Equation (43).

$$\text{s.t. } \overline{AP} = y_A(\beta) \Rightarrow \frac{bc_f^2}{2R^2} = \frac{c_f}{2}\sin(2\beta) \tag{40}$$

$$\beta = \frac{1}{2}\sin^{-1}\left(\frac{2\overline{AP}}{c_f}\right) = \frac{1}{2}\sin^{-1}\left(\frac{2}{c_f}\frac{bc_f^2}{2R^2}\right) = \frac{1}{2}\sin^{-1}\left(\frac{bc_f}{R^2}\right) \tag{41}$$

$$\text{s.t. } \overline{OP}\cos\gamma = \left(\overline{OO'}\right)_1 - x_A(\beta) + c_f$$

$$\Rightarrow \frac{c_f R}{2}\sqrt{\frac{bc_f + R^2}{b^2c_f^2 + R^4}} = \left(\overline{OO'}\right)_1 - c_f\cos^2\beta + c_f \tag{42}$$

$$\left(\overline{OO'}\right)_1 = \overline{OP}\cos\gamma - c_f + c_f\cos^2\beta = \frac{1}{2}c_f\sqrt{\frac{b^4 + b^2c_f^2 + c_f^4}{\left(b^2 + c_f^2\right)^2}} \tag{43}$$

Additional equations are:

$$\overline{O'P''} = \sqrt{x_A(\beta)^2 + y_A(\beta)^2}, \tag{44}$$

$$\overline{OP''} = \sqrt{\left(\left(\overline{OO'}\right)_1 + x_A(\beta)\right)^2 + y_A(\beta)^2}, \tag{45}$$

$$\overline{OP'} = \sqrt{\left(\left(\overline{OO'}\right)_1 + c_f - x_A(\beta)\right)^2 + y_A(\beta)^2}, \tag{46}$$

$$\overline{PP'} = \overline{OP}\cos\gamma - \left(\left(\overline{OO'}\right)_1 + c_f - x_A(\beta)\right) = 0. \tag{47}$$

where Equation (47) reduces to zero, for mathematical confirmation.

Phase 3: Constrained to Point I

The circle $r_{A''}(\theta)$ is constrained so I and I'' coincide, limiting $\overline{OO'}$ as a function of b and c_f, maintaining *two degrees of geometric freedom*. We impose $\overline{II''} = 0$ ($\overline{OI} = \overline{OI''}$), resolving into vertical and horizontal constraints. Equation (48) solves for ψ (angle of $\overline{O'I'''}$ from the abscissa) in Equation (49); Equation (50) solves for $\left(\overline{OO'}\right)_2$ in Equation (51).

$$\text{s.t. } \overline{OI}\sin\alpha = y_A(\psi) \Rightarrow \frac{bc_f^2}{R^2} = \frac{c_f}{2}\sin(2\psi) \tag{48}$$

$$\psi = \frac{1}{2}\sin^{-1}\left(\frac{2\overline{OI}\sin\alpha}{c_f}\right) = \frac{1}{2}\sin^{-1}\left(\frac{2}{c_f}\frac{bc_f^2}{R^2}\right) = \frac{1}{2}\sin^{-1}\left(\frac{2bc_f}{R^2}\right) \tag{49}$$

$$\text{s.t. } \overline{OI}\cos\alpha = \left(\overline{OO'}\right)_2 - x_A(\psi) + c_f \Rightarrow \frac{b^2c_f}{R^2} = \left(\overline{OO'}\right)_2 - c_f\cos^2\psi + c_f \tag{50}$$

$$\left(\overline{OO'}\right)_2 = \overline{OI}\cos\alpha - c_f + c_f\cos^2\psi = \frac{c_f\left(b^2 - c_f^2\right)}{b^2 + c_f^2} \tag{51}$$

Additional equations are:

$$\overline{O'I'''} = \sqrt{x_A(\psi)^2 + y_A(\psi)^2}, \tag{52}$$

$$\overline{OI'''} = \sqrt{\left(\left(\overline{OO'}\right)_2 + x_A(\psi)\right)^2 + y_A(\psi)^2}, \tag{53}$$

$$\overline{OI''} = \sqrt{\left(\left(\overline{OO'}\right)_2 + c_f - x_A(\psi)\right)^2 + y_A(\psi)^2}, \tag{54}$$

$$\overline{II''} = \overline{OI}\cos\alpha - \left(\left(\overline{OO'}\right)_2 + c_f - x_A(\psi)\right) = 0, \tag{55}$$

where Equation (55) reduces to zero, for mathematical confirmation.

Phase 4: Constrained to Points P and I

The circle $r_{A''}(\theta)$ is constrained so P and I coincide with P' and I'', respectively, limiting $\overline{OO'}$ and c_f as functions of b, reducing to *one degree of geometric freedom*. We set $\left(\overline{OO'}\right)_1 = \left(\overline{OO'}\right)_2$:

$$\left[\left(\overline{OO'}\right)_1 = \left(\overline{OO'}\right)_2\right]; \frac{1}{2}c_f\sqrt{\frac{b^4 + b^2c_f^2 + c_f^4}{\left(b^2 + c_f^2\right)^2}} = \frac{c_f\left(b^2 - c_f^2\right)}{b^2 + c_f^2}. \tag{56}$$

Solutions are $c_f = 0$ and $c_f = \pm\varphi^{-1}b$, where $\varphi = \left(1 + \sqrt{5}\right)/2 \approx 1.618$ is the golden ratio. $c_f = 0$ is trivial (geometry collapses). $c_f = -\varphi^{-1}b$ corresponds to quadrant II. Thus, we select $c_f = \varphi^{-1}b$ for quadrant I:

$$c_f = \varphi^{-1}b. \tag{57}$$

This concludes State 2, where the sine amplitude b drives full geometry crea-

tion, with the cosine amplitude c_f being constrained. Equation (57) is interestingly similar to Haramein's $k_I/k_R = \varphi^{-1}$ for the spatial decay rate of metric fluctuations regarding his recent work pertaining to an extension of Einstein-Rosen's geometric vision [20]. With this in mind and interesting to note, substitution of $c_f = \varphi^{-1}b$ into all previous equations embeds φ throughout the system (as shown in **Appendix A**).

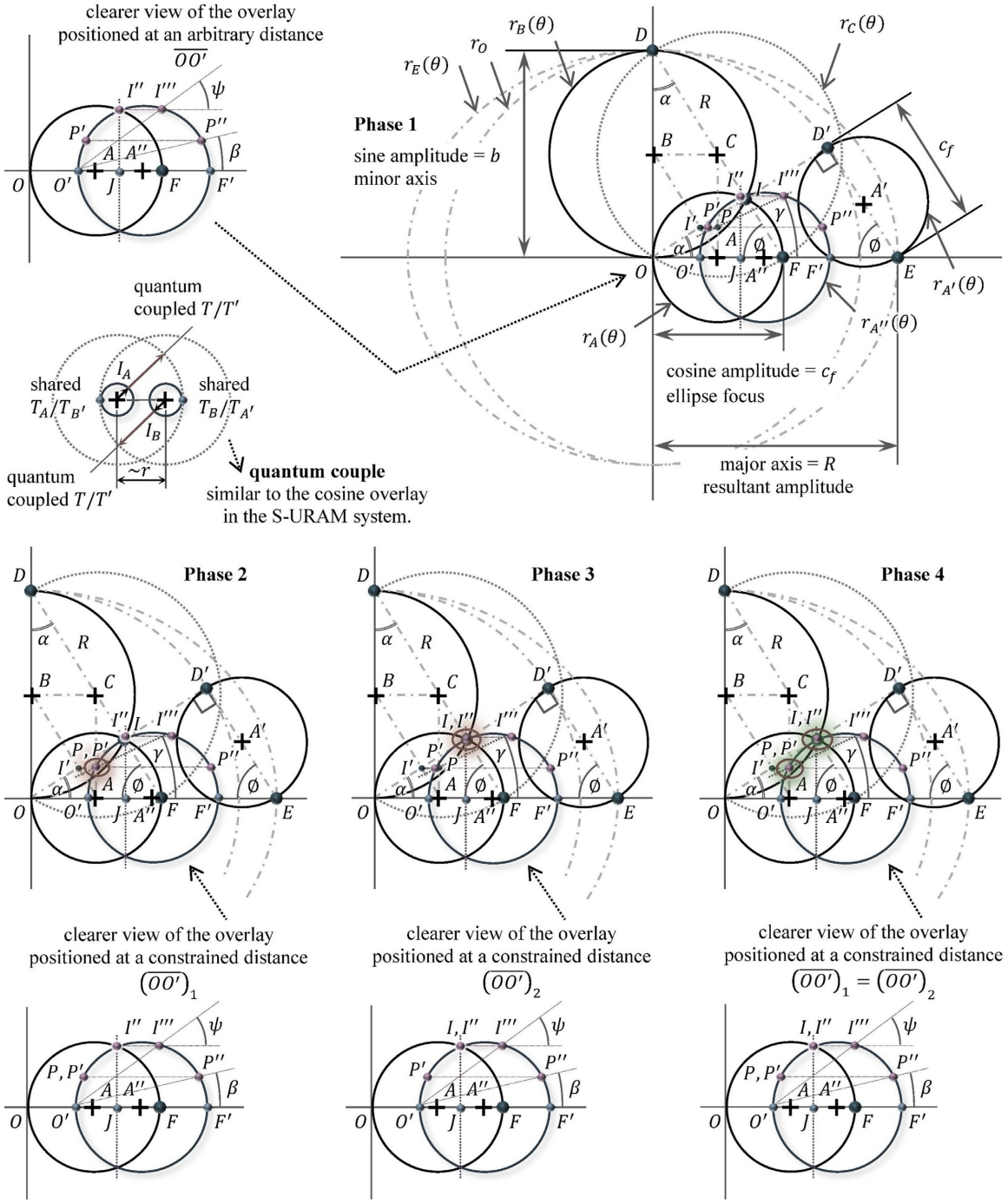

Figure 2. (Phase 1) Free radial cosine overlay, (Phase 2) Radial cosine overlay constrained to cross point P, (Phase 3) Radial cosine overlay constrained to cross point I, (Phase 4) Final radial cosine overlay constrained to cross points P and I.

2.3. Connection with 2D Hexagonal-Shaped View of the Cuboctahedron

The cuboctahedron (12 vertices, 24 edges, 14 faces) relates to quantum gravity and spacetime in Haramein-Rauscher topology, emerging from modified Einstein Field Equations (EFE) and Grand Unified Theory (GUT) via U_4 topology—dual torus, $U_4 = U_1 \times U_1 \times U_1 \times U_1$, where U_1 is the Weyl (photon/electromagnetic) gauge invariance group—and the octahedral subset (maximal compact space/cover group) of $C\left[\bar{O}\right]$ and $C[O]$ spaces. Including torque and Coriolis force terms may unify gravity with strong, weak, and electromagnetic forces [6]. This approach represents the dense tangent packing of 13 Planck Spherical Units (PSUs) in Quantum Gravity & Holographic Mass (QGHM) [16–20]. Its 2D hexagonal view packs 7 spheres.

From Figure 2, a partial hexagon emerges from lines connecting B, C, and A. As illustrated in Figure 3, scaling this hexagon shows that its side s and source circle diameter $2\times\overline{OO'}$ are in golden ratio, as likewise for the sine and cosine amplitudes.

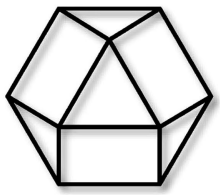

cuboctahedron
8 triangles = octahedron
6 squares = cube = hexahedron
8 trig + 6 sqr = cuboctahedron

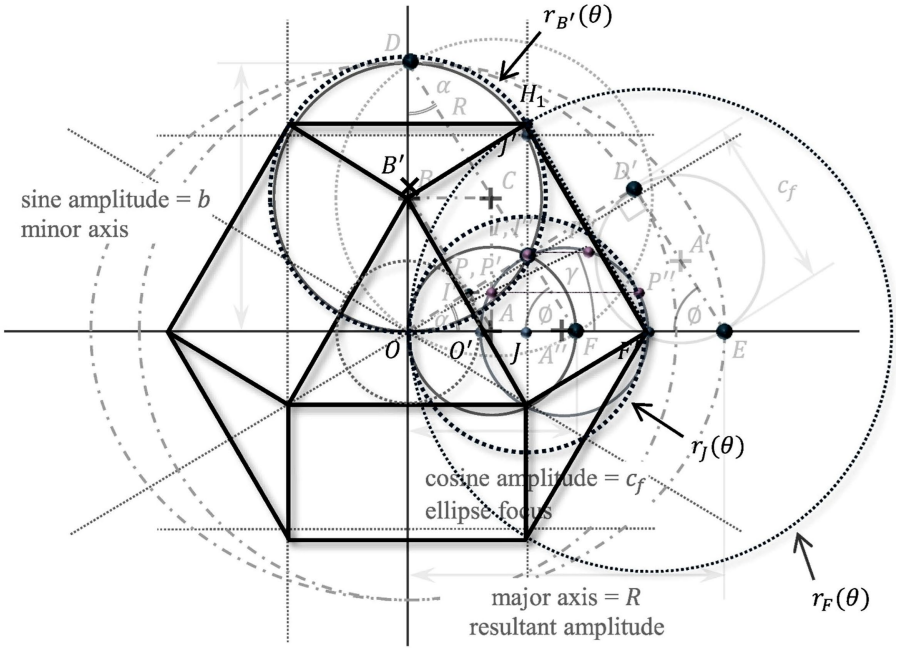

Figure 3. 2D View of the cuboctahedron constructed from S-URAM waves and the direct S-URAM wave construction.

Horizontal and vertical construction lines intersect $r_B(\theta)$ at J', vertically aligned with J. Reflecting across axes forms a symmetric foundation. Line $\overline{OF'}$ rotates about F' to create circle $r_{F'}(\theta)$:

$$r_{F'}(\theta) = 2\overline{OF'}\cos\theta = 2\left(\overline{OJ} + \overline{JF'}\right)\cos\theta = 4\overline{OI}\cos\alpha\cos\theta = \frac{4b^2 c_f}{R^2}\cos\theta, \quad (58)$$

$$x_{F'}(\theta) = r_{F'}(\theta)\cos\theta = \left(\frac{4b^2 c_f}{R^2}\cos\theta\right)\cos\theta = \frac{4b^2 c_f}{R^2}\cos^2\theta, \quad (59)$$

$$y_{F'}(\theta)=r_{F'}(\theta)\sin\theta=\left(\frac{4b^2c_f}{R^2}\cos\theta\right)\sin\theta=\frac{2b^2c_f}{R^2}\sin(2\theta). \tag{60}$$

This intersects the vertical line at H_1, and $\overline{F'H_1}$ forms a 60˚ edge. Reflecting across quadrants completes the equilateral hexagon, forming the 2D-cuboctahedron perimeter. An interior equilateral triangle (side = hexagon side) is centered at O, and lines connect between the triangle and hexagon's vertices to complete the 2D cuboctahedron projection. Equation (62) verifies $s/\left(2\overline{OO'}\right)=\varphi$:

$$s=\overline{F'H_1}=\left(\overline{OJ}+\overline{JF'}\right)\cos\alpha=2\overline{OI}\cos\alpha=\frac{2b^2c_f}{R^2}, \tag{61}$$

$$\frac{s}{2\overline{OO'}}=\frac{2b^2c_f/R^2}{2c_f\left(b^2-c_f^2\right)/R^2}=\frac{b^2}{b^2-c_f^2}=\frac{b^2}{b^2\left(1-\left(\varphi^{-1}\right)^2\right)}=\frac{1}{1-\left(\varphi^{-1}\right)^2}\equiv\varphi. \tag{62}$$

2.4. Directly Connected S-URAM Geometry Emergence

A simplified S-URAM geometry emerges, with equations in terms of φ, forming curves that intersect hexagonal symmetries. This suggests standalone hexagons are embedded with φ as a function of b (see **Appendix B**), potentially connecting with scaling laws and the Planck length, inspired by Haramein, Wheeler, *et al.* [20] [60] [61].

For S-URAM waves (**Figure 3**), $r_J(\theta)$, $r_{B'}(\theta)$, and $r_{C'}(\theta)$ are:

$$r_{B'}(\theta)=\frac{2\overline{OI}\cos\alpha}{\sin 60^\circ}\sin\theta=\left(\frac{4}{\sqrt{3}}\overline{OI}\cos\alpha\right)\sin\theta=\frac{4b^2c_f}{\sqrt{3}R^2}\sin\theta, \tag{63}$$

$$r_J(\theta)=\left(2\overline{OI}\cos\alpha\right)\cos\theta=\frac{2b^2c_f}{R^2}\cos\theta, \tag{64}$$

$$r_{C'}(\theta)=\hat{R}R_N\cos\left(\theta+\hat{\varnothing}\varnothing_N\right)=R_N\cos\left(\theta-\varnothing_N\right), \tag{65}$$

$$R_N=\sqrt{\left(2\overline{OI}\cos\alpha\right)^2+\left(\frac{4}{\sqrt{3}}\overline{OI}\cos\alpha\right)^2}=\frac{2\sqrt{21}}{3}\overline{OI}\cos\alpha=\frac{2\sqrt{21}}{3}\frac{b^2c_f}{R^2}, \tag{66}$$

$$\varnothing_N=\tan^{-1}\left(\frac{\left(4/\sqrt{3}\right)\overline{OI}\cos\alpha}{2\overline{OI}\cos\alpha}\right)=\tan^{-1}\left(2\sqrt{3}/3\right). \tag{67}$$

2.5. Conversion of Line $\overline{OO'}$ to a Specified Driving Variable along with Conversion of Sine Amplitude b to a Driven Variable

$\overline{OO'}$ is critical in State 2/Phase 4. With $s/\left(2\overline{OO'}\right)=\varphi$, setting diameter $2\times\overline{OO'}$ to 1 m yields $s\approx 1.618$ m. Equation (69) expresses b as a function of radius $r=\overline{OO'}$, where r could be 0.5 m, 10 m, or whatever one desires to scale it to, such as the Planck radius $\ell/2$ ($\ell\approx 1.62\times10^{-35}$ m) [17].

$$r=\overline{OO'}=\frac{c_f\left(b^2-c_f^2\right)}{b^2+c_f^2}=\frac{\sqrt{1+\varphi^2+\varphi^4}}{2\varphi\left(1+\varphi^2\right)}b=\frac{b}{\varphi+2} \tag{68}$$

$$b = \frac{2\varphi\left(1+\varphi^2\right)}{\sqrt{1+\varphi^2+\varphi^4}} r = \left(\varphi+2\right) r \tag{69}$$

From Equation (69), **Appendix A** compiles key equations for graphing S-URAM geometry with golden ratio reductions. **Appendix B** explores generalizations for deeper insights.

2.6. Symmetric Geometry & Recursively Scaled Geometries

Fractals and recursive scaling are central to unified field theories [20] [30] [31] [41]-[45]. Fractal concepts, introduced by Mandelbrot, have found applications in modeling complex structures across a range of cosmic and quantum contexts, particularly where self-similarity and scale invariance are observed [23]. These structures provide a framework for understanding phenomena that exhibit patterns repeating over multiple scales, from the clustering of galaxies to quantum fluctuations. S-URAM's scaling principles may illuminate such self-similar behavior in the cosmos or matter distribution, offering a geometric and recursive perspective on natural hierarchies. Moreover, these principles could be relevant to diverse areas including turbulence, critical phenomena, and complex network interactions [6] [20] [30], providing a unified lens to connect macro- and microscopic structures within a single theoretical framework.

Haramein posits a recursive, self-similar universe evolving from entropy dynamics and the conservation of momentum over billions of years, with PSU interactions that lead to Einstein's General Theory of Relativity [6] [16]-[20]. This aligns with Wheeler: "*The vision of quantum gravity is a vision of turbulence—turbulent space, turbulent time, turbulent spacetime… spacetime in small enough regions should not be merely 'bumpy', not merely erratic in its curvature, it should fractionate into ever-changing, multiply-connected geometries*" [58].

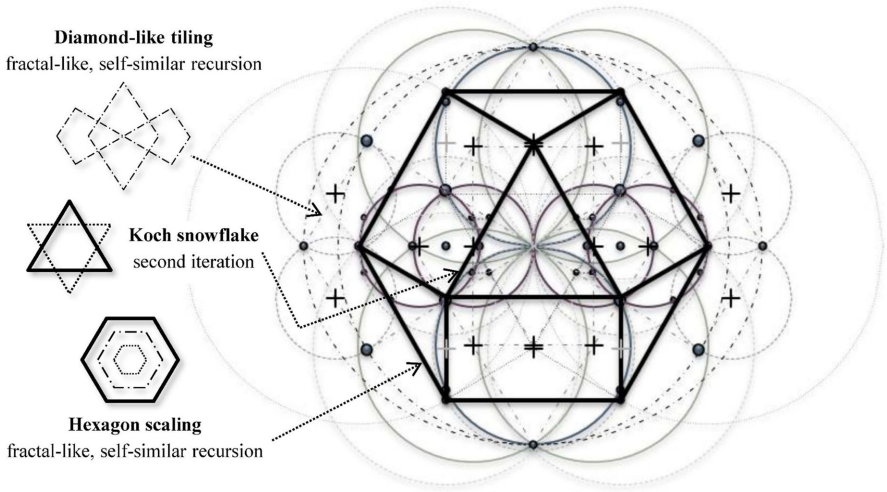

Figure 4. Symmetric geometry and basis for recursively scaled geometries.

Figure 4 above shows a symmetric configuration by reflecting points, lines, and

circles across quadrants, revealing self-contained, multi-scale shapes (circles, diamonds, hexagons). Ratios enable recursive scaling of b. The bold hexagon contains a second iteration of the Koch-snowflake comprised of a smaller hexagon, exhibiting fractal-like properties with infinite recursion.

This suggests scaling techniques for an infinite self-similar fabric, connecting to Haramein-Rauscher topology or other spacetime frameworks as per Haramein's wavenumber/amplitude ratio, Zhou's half-wavelengths for α approximations, and the Mandelbrot set due to its infinite fractality [6] [20] [23] [55].

3. Results Discussion

3.1. Validation

To validate the geometric constructs derived from the Simulated Unified Resultant Amplitude Method, we employed the full set of polar and parametric wave equations to generate computer-based scatter plots (**Figure 5** below). These visualizations utilized 16 points (not shown) per S-URAM circle and 32 points (not shown)

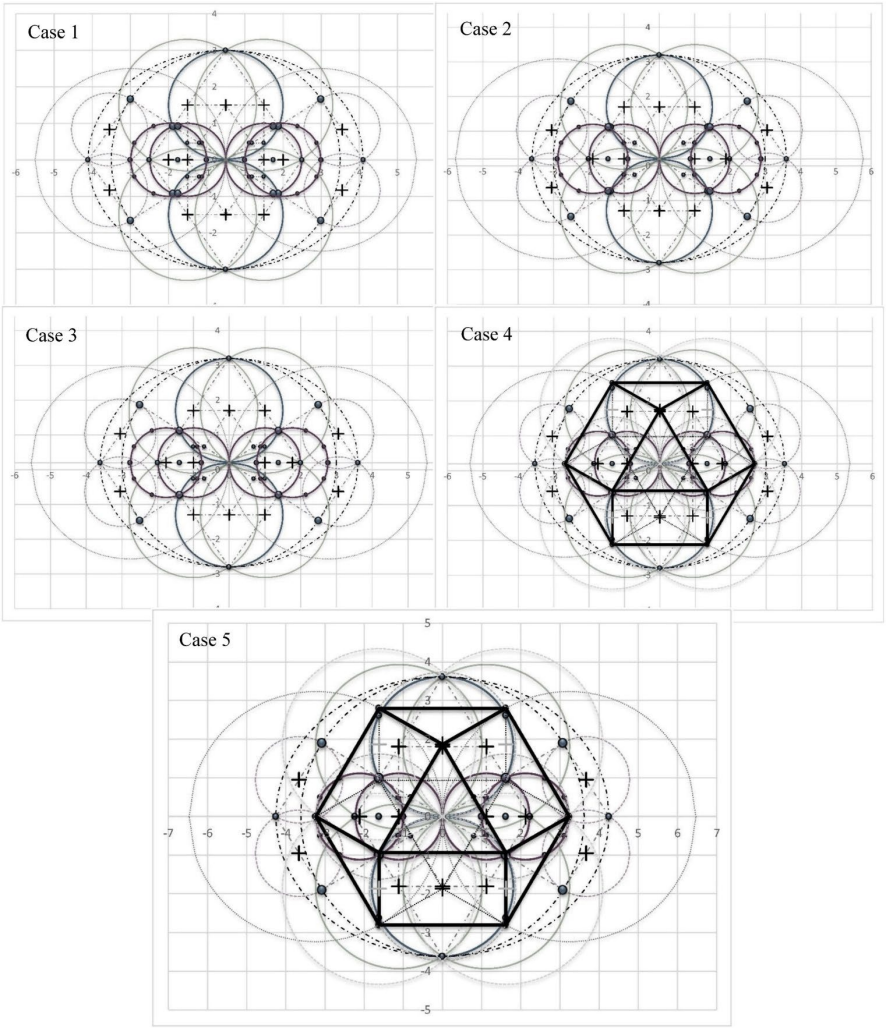

Figure 5. Computer-generated scatter plot for graphical validation.

for the circle and ellipse centered at origin O. Additional Cartesian lines, coordinates, and point markers (sphere and "+" symbols, the latter denoting circle centers) were incorporated to highlight critical intersection points and emergent structures, including Euclid's triangle, the regular hexagon, equilateral triangles, and the overall 2D hexagonal projection of the cuboctahedron (Figure 4).

For rigorous numerical evaluation, five distinct scenarios were defined (Table 1), representing varying degrees of geometric freedom through the application or relaxation of constraints on critical intersection points.

Table 1. Scenarios for graphical validation.

Scenarios	Sine Amplitude b		Cosine Amplitude c_f		Source Circle Radius r	
1	Given	3 m	Given	2 m	Given	0.5 m
2	Given	3 m	Given	2 m	Driven[a]	~0.887 m
3	Given	3 m	Given	2 m	Driven[a]	~0.769 m
4	Given	3 m	Driven[b]	~1.854 m	Driven[a]	~0.829 m
5	Driven[c]	~3.618 m	Driven[b]	~2.236 m	Given	1 m

a. Equations (43), (51), and (68) are used for respective "driven" cases of r; b. Equation (57) is used for both "driven" cases of c_f; c. Equation (69) is used for "driven" case of b.

Scatter plots for all scenarios are shown in Figure 5, confirming adherence to theoretical expectations:

Scenario 1. (*Three Degrees of Geometric Freedom*): Removal of constraints yield non-intersection of the cosine overlay with points P and I, as predicted.

Scenario 2. (*Two Degrees of Geometric Freedom with First Constraint* $\overline{PP'}=0$): Cosine overlay intersects only P.

Scenario 3. (*Two Degrees of Geometric Freedom with Second Constraint* $\overline{II''}=0$): Cosine overlay intersects only I.

Scenario 4. (*One Degree of Geometric Freedom with Combined Constraints Based on Given Sine Amplitude*): Both P and I intersected.

Scenario 5. (*One Degree of Geometric Freedom with Combined Constraints Based on the Given Source Circle Radius*): Both P and I intersected, with driven parameters yielding values evocative of golden-ratio scaling (e.g., ~3.618 m and ~2.236 m essentially equivalent to φ^2+1 and $\varphi^{-1}\left(\varphi^2+1\right)$).

Across all scenarios, consistent emergent features validate the model:

1) *Resultant wave intersections at origin/peak points of the sine and cosine waves.*

2) *Sine and cosine wave alignment/intersection with hexagonal symmetries.*

3) *Line orthogonality, Euclid triangle similarities, etc.*

Importantly, the agreement between analytic predictions and graphical realizations persists across multiple constraint regimes, indicating robustness to parameter variation. By explicitly relaxing and reapplying geometric constraints across

five scenarios, the analysis functions as a sensitivity test, demonstrating that the emergent symmetries are structurally stable features of the formulation rather than fine-tuned consequences of particular amplitude or radius selections.

These features not only confirm the mathematical robustness of S-URAM but also reveal precise golden-ratio (φ) proportions in hexagonal side lengths relative to the source circle diameter—directly mirroring the symmetric properties of the cuboctahedron's 2D projection. Furthermore, the constrained scenarios (4 and 5) produce amplitude and radius values numerically exact and proportional to powers of φ, underscoring the inherent self-similar scaling.

Symmetric reflection and multiplicative expansions of these patterns exhibit fractal-like recursion, with iterative overlays resembling projections of the second iteration of the Koch snowflake. This recursive self-similarity aligns with the broader implications for unified physics: the emergent cuboctahedral-hexagonal geometry echoes Haramein-Rauscher modifications to Einstein's Field Equations through incorporating torque/Coriolis effects, while the golden-ratio embedding and fractal characteristics suggest conceptual parallels to scalable spacetime structures in Quantum Gravity & Holographic Mass frameworks. Thus, these validated simulations provide empirical support for S-URAM as a potential geometric bridge between wave superposition dynamics and polyhedral symmetries central to ongoing unification efforts.

3.2. Toward a Field-Theoretic Interpretation

As noted in the Introduction: Scope and Limitations, S-URAM is a geometric framework complementary to established theories, not a replacement. It does not explicitly address renormalization (e.g., running couplings via beta functions) or spontaneous symmetry breaking (SSB) in gauge theories like $\mathrm{SU}(2)_{\mathrm{L}} \times \mathrm{U}(1)_{\mathrm{Y}}$. However, conceptual parallels exist: fractal recursion (Section 2.6) may mimic renormalization group flows through φ-scaled iterations, while PSU packing asymmetries (**Appendices E-F**) could analogize SSB via volumetric perturbations in cuboctahedral lattices [6] [9]. Future extensions could embed non-Abelian multi-wave superpositions to model these, bridging the gap to Standard Model dynamics without superseding them.

To provide a field-theoretic context for the geometric constraints developed in Sections 2-3 and **Appendices C-F**, we present an illustrative effective Lagrangian density inspired by the Simulated Unified Resultant Amplitude Method (S-URAM). This formulation is phenomenological and conceptual, mapping key S-URAM parameters (e.g., amplitudes b, $c_f = \varphi^{-1} b$, phase $\varnothing = \tan^{-1}(\varphi)$, resultant R) onto scalar and vector fields. It is not a rigorous quantum field theory but illustrates how emergent couplings may arise from wave superposition dynamics with complex amplitudes and phase interference.

We introduce a complex scalar field $\phi(x)$ representing normalized amplitude fluctuations in S-URAM wave overlays (e.g., $\phi \sim \left(b \sin\theta + c_f \mathrm{e}^{-\mathrm{i}\varnothing} \cos(\theta - \varnothing)\right)/R$, rendered dimensionless, with inherent phase structure from Euler's formula and

interference patterns) and an Abelian vector field $A_\mu(x)$ analogizing rotational "twist" from golden-ratio constraints. The proposed Lagrangian density is:

$$\mathcal{L}_{\text{S-URAM}} = \left(\partial^\mu \phi^*\right)\left(\partial_\mu \phi\right) - V\left(\phi^* \phi\right) - \frac{1}{4} F_{\mu\nu} F^{\mu\nu} + g_{\text{eff}} J^\mu A_\mu, \tag{70}$$

where $F_{\mu\nu} = \partial_\mu A_\nu - \partial_\nu A_\mu$ is the field strength tensor, and $J^\mu = \mathrm{i}\left(\phi^* \partial^\mu \leftrightarrow \phi\right) = \mathrm{i}\left(\phi^* \partial^\mu \phi - \phi \partial^\mu \phi^*\right)$ is the standard conserved Noether current for global $\mathrm{U}(1)$ phase invariance, directly derived from interference patterns in constructive/destructive wave summation (phase gradients driving charge flow). The potential $V\left(\phi^* \phi\right)$ encodes golden-ratio self-similarity and fractal recursion (Section 2.6):

$$V\left(\phi^* \phi\right) = m^2 |\phi|^2 + \lambda\left(|\phi|^2\right)^2 + \sum_{n=1}^{N} \kappa_n \frac{\left(|\phi|^2\right)^{n+1}}{\phi^n}, \tag{71}$$

with $\varphi = \left(1+\sqrt{5}\right)/2 \approx 1.618034$. Parameters are motivated geometrically:

1) $m^2 \propto 1/R^2$ (inverse resultant amplitude scaling from Equation (13)),

2) $\lambda \approx 1/13$ (volumetric stiffness from 13-PSU packing; **Appendix E**),

3) $\kappa_n \propto (\pm 1)/\varphi^{2n+1}$ (recursive coefficients from phase deviations $\Delta\varnothing$ and higher-order fractal terms, e.g., $\kappa_1 \sim \varphi^{-1}$ for golden contraction, $\kappa_3 \sim -\varphi^{-5}$ for quintic correction; **Appendices D-F**).

This potential yields minima at $|\phi|^2 \sim \varphi^k$, reflecting discrete hierarchical scaling in PSU lattices. The effective coupling g_{eff} emerges from minimization under cuboctahedral constraints and is uniformly defined as the inverse effective strength (for dimensionlessness and consistency across interactions), using full refined expressions from **Appendices D-F**:

$$g_{\text{eff}} \approx \begin{cases} \dfrac{360}{\varphi^2} - \dfrac{2}{\varphi^3} + \dfrac{1}{(3\varphi)^5} & \left(\text{electromagnetic : refined rotational twist}\right) \\ \dfrac{1}{3/\left(13 - 1/\left(3\varphi^5\right)\right)} & \left(\text{weak : refined chiral/volumetric asymmetry}\right) \\ 8 + \varphi^{-1} - \varphi^{-5} & \left(\text{strong : refined gluon-edge multiplicity}\right) \end{cases} \tag{72}$$

These values approximate the known inverse couplings at a characteristic scale (vacuum-like values analogous to renormalization scales in torque/Coriolis-extended modified Einstein field equations [6]):

1) Electromagnetic: $g_{\text{eff}} \approx 137.036$ (close to $\alpha^{-1} \approx 137.035999$ from recent measurements),

2) Electroweak: $g_{\text{eff}} \approx 4.323$ (corresponding to $1/\sin^2 \theta_W \approx 4.323$),

3) Strong: $g_{\text{eff}} \approx 8.528$ (close to $\alpha_s^{-1} \approx 8.528$ in the relevant regime).

This illustrative framework highlights how S-URAM's wave constraints and polyhedral symmetries could generate gauge-like interactions via amplitude/phase asymmetries, complementing holographic principles [16]-[20]. The use of a complex scalar ensures proper $\mathrm{U}(1)$ invariance and a conserved current rooted in wave interference, aligning with the model's emphasis on constructive/destructive summation and golden-ratio phases. Future non-Abelian extensions (e.g., multi-

component fields for $SU(3)_C$ gluon octets) might incorporate renormalization through fractal-inspired beta functions. The model remains exploratory and aligns with the phenomenological scope outlined in the Introduction.

4. Conclusions

This exploratory study demonstrates that the Simulated Unified Resultant Amplitude Method (S-URAM) generates geometric patterns through which the hexagonal projection of the cuboctahedron emerges with exact golden-ratio proportions. Notably, φ appears precisely in the relationships between sine and cosine amplitudes and in the ratio of the hexagonal side length to the diameter of the source circle. Scatter plot analyses further validate the model, confirming close alignment between simulated and expected geometric behaviors.

These results align with and extend prior work in Haramein-Rauscher topology, revealing a deep geometric correspondence between S-URAM wave dynamics, cuboctahedral symmetry, golden-ratio scaling, and fractal-like recursion—within the broader contexts of modified Einstein field equations, grand unified theories, and the Quantum Gravity & Holographic Mass framework. The derivation of a base approximate expression for the fine-structure constant from 2D constraints (**Appendix C**), refined in 3D to exceptional precision (matching CODATA to ~10^{-10} error; **Appendix D**), together with parallel geometric approximations of the weak mixing angle from phase asymmetries and 13-PSU packing (**Appendix E**) and the strong coupling constant from edge multiplicity and recursive scaling (**Appendix F**), further underscores the potential of S-URAM to derive both electromagnetic, electroweak, and strong parameters geometrically. Collectively, the findings point toward a scalable geometric paradigm that may illuminate interconnections among quantum mechanics, general relativity, and fundamental physical constants.

While the methodology outlined in this paper presents exciting potential for geometrically-based unification, it is important to reiterate the preliminary nature of such rather than the presentment of a final unified theory. Consequently, the results presented within this study should be interpreted within the conceptual and phenomenological scope outlined in the Introduction. Future work, particularly experimental validation and collaboration with theoretical physicists, will be crucial to assess the viability and implications of this model within the context of current physical theories. Nevertheless, and although significant questions remain unresolved, the geometric approach entailed herein provides a unique and promising theoretical foundation and associated mathematical simulation proposal/conceptual model for future investigations into the underlying structural principles of the universe.

5. Future Research

The geometric patterns emerging from the Simulated Unified Resultant Amplitude Method (S-URAM)—particularly the golden-ratio-proportioned hexagonal

projections of the cuboctahedron and their fractal-like scaling—suggest several avenues for extending this work within unified physics frameworks. Future research could involve empirical testing of the geometric structures proposed, with particular attention to how the fine-structure constant and other fundamental constants may be derived from the self-similar, fractal-like patterns suggested by the associated models contained herein. However, and again, the results should be viewed as preliminary, with the recognition that further theoretical and experimental work will be necessary to validate or refine these concepts.

Nevertheless, and in connection, a primary direction involves deeper exploration of the golden ratio (φ) in relation to dimensionless constants, such as the fine-structure constant (α), the weak mixing angle (θ_W), and the strong coupling constant (α_s). Prior studies have noted numerical approximations linking φ to α^{-1} through harmonic proportions or geometric models [25] [26]. Integrating these ideas with S-URAM dynamics could yield new insights into how self-similar wave superpositions might inform scaling behaviors in quantum electrodynamics (QED), electroweak unification, QCD running, or holographic mass formulations [17] [62]. Building on the high-precision 3D derivation of α (**Appendix D**), the electroweak extension (**Appendix E**), and the strong-force approximation (**Appendix F**), further refinements could incorporate quartic or higher φ terms to explore QCD ties or exact CODATA matching [5] [56].

Further research could employ advanced computational tools to model three-dimensional S-URAM constructions beyond the initial extension, examining fuller cuboctahedral packing of Planck spherical units and potential alignments with Quantum Gravity & Holographic Mass predictions, including chiral asymmetries for $\mathrm{SU}(2)_{\mathrm{L}} \times \mathrm{U}(1)_{\mathrm{Y}}$ embedding and color-flow dynamics for $\mathrm{SU}(3)_{\mathrm{C}}$ [9]. Such models might predict testable signatures in astrophysical phenomena, including cosmic microwave background anisotropies, galactic clustering, or large-scale fractal distributions [41]-[45].

To further assess the distinctions of the S-URAM framework from the Standard Model and evaluate its phenomenological implications, specific testable predictions can be examined. For instance: (1) ultra-precision measurements in atomic interferometry or hydrogen spectroscopy could search for deviations from CODATA values at the level of golden-ratio-scaled corrections (~10^{-10} in α)—absence of such signatures beyond experimental uncertainties would constrain the proposed geometric embedding of the fine-structure constant; (2) analyses of cosmic microwave background anisotropies for signatures of fractal cuboctahedral patterns (e.g., angular correlations modulated at multiples of φ) could probe PSU-based interpretations—non-detection at current resolutions would limit such granular spacetime models; (3) lattice QCD simulations incorporating cuboctahedral symmetry constraints could test whether the running of α_s deviates from PDG fits by more than ~1%, potentially falsifying the proposed strong-force edge-multiplicity ties.

Additionally, incorporating S-URAM geometries into quantum field theory simulations—particularly those exploring electromagnetic-gravitational and weak in-

teractions in curved spacetime—could bridge conceptual gaps between quantum mechanics and general relativity [1]-[6] [13]-[15]. Interdisciplinary efforts combining mathematics, theoretical physics, and cosmology would be valuable, potentially applying these scalable, self-similar structures to fractal cosmology or hierarchical models of spacetime, including empirical validation of the 3D α and electroweak expressions through angular distributions or spectral data [36] [37] [39].

Ultimately, these investigations may contribute to ongoing discussions on geometric unification, offering fresh perspectives on the interplay of wave dynamics, polyhedral symmetry, and natural constants without presupposing revolutionary technological outcomes. While remaining conjectural at this stage, advancements in our understanding of fundamental symmetries and geometric structures could indirectly inform breakthroughs in zero-point energy concepts, gravitational modeling, and biomedical applications. By maintaining mathematical and simulational rigor, future work can build incrementally on the foundational patterns identified herein, progressively refining or reinterpreting them in light of new theoretical insights and experimental evidence.

Acknowledgements

ChatGPT (OpenAI) assisted in drafting Results Validation Section 3.2 and **Appendices D-F** and in suggesting phrasing for related sections of the main text for ensuring consistency with the aforementioned section and appendices. All content was critically reviewed, revised, integrated, and finalized by the author.

Conflicts of Interest

The author declares no conflicts of interest regarding the publication of this work.

References

[1] Wheeler, J.A. (1990) Information, Physics, Quantum: The Search for Links. In: Zurek, W.H., Ed., *Complexity, Entropy, and the Physics of Information*, Addison-Wesley, 3-28.

[2] Weinberg, S. (1995) The Quantum Theory of Fields (Vol. 1). Cambridge University Press. https://doi.org/10.1017/cbo9781139644167

[3] Rovelli, C. (2004) Quantum Gravity. Cambridge University Press. https://doi.org/10.1017/cbo9780511755804

[4] Barbour, J. (1999) The End of Time. Oxford University Press.

[5] Kreshchuk, M. (2021) Quantum Simulation of Quantum Field Theory in the Front Form. Ph.D. Dissertation, Tufts University.

[6] Haramein, N. and Rauscher, E.A. (2005) The Origin of Spin: A Consideration of Torque and Coriolis Forces in Einstein's Field Equations and Grand Unification Theory. In: Amoroso, R.L., Lehnrt, B. and Vigier, J.P., (Eds.), *Beyond the Standard Model: Searching for Unity in Physics*, The Noetic Press, 153-168.

[7] Coldea, R., Tennant, D. A., Wheeler, E. M., Wawrzynska, E., Prabhakaran, D., Telling, M., Habicht, K., Smeibidl, P. and Kiefer, K. (2010) Quantum Criticality in an Ising Chain: Experimental Evidence for Emergent E_8 Symmetry. *Science*, **327**, 177-180. https://doi.org/10.1126/science.1180085

[8] Coldea, R., Tennant, D.A., Wheeler, E.M., Wawrzynska, E., Prabhakaran, D., Telling, M., *et al*. (2010) Observation of Universal Bound State Spectrum Near a Magnetic Quantum Critical Point. *Science*, **327**, 177. https://doi.org/10.36471/JCCM_March_2010_02

[9] Gioia, L. and Thorngren, R. (2025) Exact Chiral Symmetries of 3+1D Hamiltonian Lattice Fermions. https://arXiv:2503.07708v2

[10] Buckminster Fuller, R. (1975) Synergetics: Explorations in the Geometry of Thinking. Macmillan.

[11] Critchlow, K. (2007) Time Stands Still: New Light on Megalithic Science. Gordon Fraser.

[12] Einstein, A. (1915) Die feldgleichungen der gravitation. Sitzungsberichte der Königlich Preußischen Akademie der Wissenschaften, 844-847.

[13] Einstein, A. (1930) The Field Equations of Gravitation. Wikisource.

[14] Janssen, M. and Renn, J. (2004) Untying the Knot: How Einstein Found His Way Back to Field Equations Discarded in the Zurich Notebook. Preprint.

[15] Schwarzschild, K. (1916) On the Gravitational Field of a Mass Point According to Einstein's Theory (S. Antoci and A. Loinger, Trans.). 189-196. https://arxiv.org/abs/physics/9905030v1

[16] Haramein, N. and Dubois, D.M. (2010) The Schwarzschild Proton. *AIP Conference Proceedings*, **1303**, 95-100. https://doi.org/10.1063/1.3527190

[17] Haramein, N. (2013) Quantum Gravity and Holographic Mass. *Physical Review and Research International*, **3**, 270-292.

[18] Val Baker, A.K.F., Haramein, N. and Alirol, O. (2019) The Electron and the Holographic Mass Solution[a]. *Physics Essays*, **32**, 255-262. https://doi.org/10.4006/0836-1398-32.2.255

[19] Haramein, N., Guermonprez, C. and Alirol, O. (2024) The Origin of Mass and the Nature of Gravity. International Space Federation Laboratory, 1-52.

[20] Haramein, N., Alirol, O. and Guermonprez, C. (2025) Extending Einstein-Rosen's Geometric Vision: Vacuum Fluctuations-Induced Curvature as the Source of Mass, Gravity and Nuclear Confinement. MDPI Preprint.

[21] Kaku, M. (1994) Hyperspace: A Scientific Odyssey Through Parallel Universes, Time Warps, and the 10th Dimension. Oxford University Press.

[22] Feynman, R.P., Leighton, R.B. and Sands, M. (2011) The Feynman Lectures on Physics (Vol. 1). Basic Books.

[23] Mandelbrot, B. (1982) The Fractal Geometry of Nature. W.H. Freeman.

[24] Livio, M. (2002) The Golden Ratio: The Story of Phi, the World's Most Astonishing Number. Broadway Books.

[25] Stakhov, A.P. (2008) The Mathematics of Harmony: Clarifying the Origins and Development of Mathematics. *Journal "Congressus Numerantium"*, **193**, 5-48.

[26] Stakhov, A. and Aranson, S. (2017) The Mathematics of Harmony and "Golden" Non-Euclidean Geometry as the "Golden" Paradigm of Modern Science, Geometry, and Computer Science. *International Journal of Applied & Experimental Mathematics*, 2, Article No. 113.

[27] Pletser, V. (2018) Fibonacci Numbers and the Golden Ratio in Biology, Physics, Astrophysics, Chemistry and Technology: A Non-Exhaustive Review. https://arxiv.org/abs/1801.01369

[28] Sacco, R.G. (2018) Fibonacci Harmonics: A New Mathematical Model of Synchronicity. *Applied Mathematics*, **9**, 702-718. https://doi.org/10.4236/am.2018.96048

[29] Cruz, N., Olivares, M. and Villanueva, J.R. (2017) The Golden Ratio in Schwarzschild-Kottler Black Holes. *The European Physical Journal C*, **77**, Article No. 123. https://doi.org/10.1140/epjc/s10052-017-4670-7

[30] Haramein, N., Brown, W.D. and Val Baker, A. (2016) The Unified Spacememory Network: From Cosmogenesis to Consciousness. *NeuroQuantology*, **14**, 1-15. https://doi.org/10.14704/nq.2016.14.4.961

[31] Brown, W. (2019) Unified Physics and the Entanglement Nexus of Awareness. *NeuroQuantology*, **17**, 40-52. https://doi.org/10.14704/nq.2019.17.7.2519

[32] Stakhov, A.P. (2013) Hilbert's Fourth Problem: Searching for Harmonic Hyperbolic Worlds of Nature. *Journal of Applied Mathematics and Physics*, **1**, 60-66. https://doi.org/10.4236/jamp.2013.13010

[33] Pashaev, O. K. and Nalci, S. (2018). Golden Quantum Oscillator and Binet-Fibonacci calculus. *Journal of Physics A*: *Mathematical and Theoretical*, **45**, Article 015303. https://arxiv.org/abs/1107.4389

[34] Khen, V.P. and Khen, A.V. (2025) Heron's Triangles, Golden Section and Quantization of Decays of Scalar, Strange Mesons and Δ, N Baryons in the Hyperbolic Lobachevsky Velocity Space. *Journal of Applied Mathematics and Physics*, **13**, 3337-3351. https://doi.org/10.4236/jamp.2025.1310192

[35] Austin, R.W. (2025) NUVO Quantization I: Scalar Coherence and the Quantum of Action. *Journal of Applied Mathematics and Physics*, **13**, 3902-3912. https://doi.org/10.4236/jamp.2025.1311218

[36] Heyrovska, R. (2013) Golden Ratio Based Fine Structure Constant and Rydberg Constant for Hydrogen Spectra. *International Journal of Sciences*, **2**, 28-31.

[37] Heyrovska, R. and Narayan, S. (2005) Fine-Structure Constant, Anomalous Magnetic Moment, Relativity Factor and the Golden Ratio that Divides the Bohr Radius. arXiv preprint physics/0509207. https://arxiv.org/abs/physics/0509207

[38] Stakhov, A. and Aranson, S. (2016) The Fine-Structure Constant as the Physical-Mathematical Millennium Problem. *Physical Science International Journal*, **9**, 1-36. https://doi.org/10.9734/psij/2016/21966

[39] Sherbon, M.A. (2017) Fundamental Physics and the Fine-Structure Constant. *International Journal of Geometric Methods in Modern Physics*, **5**, 46-48.

[40] Sherbon, M.A. (2018) Fine-Structure Constant from Golden Ratio Geometry. *International Journal of Mathematics and Physical Sciences Research*, **5**, 89-100. https://doi.org/10.2139/ssrn.3148761

[41] Barabási, A.-L. and Stanley, H.E. (1995) Fractal Concepts in Surface Growth. Cambridge University Press. https://doi.org/10.1017/cbo9780511599798

[42] El Naschie, M.S. (2004) A Review of E Infinity Theory and the Mass Spectrum of High Energy Particle Physics. *Chaos*, *Solitons & Fractals*, **19**, 209-236. https://doi.org/10.1016/s0960-0779(03)00278-9

[43] Ghorbani B. (2025) Unified Fractal Field Equations as an Alternative to Einstein's General Relativity: A Comparative Mathematical Analysis. https://doi.org/10.13140/RG.2.2.19937.62568

[44] Sogukpinar, H. (2025) Fractal Spacetime and Unified Φ-Ψ Fields: A Comprehensive Framework for Matter, Forces, and the Universe in the Unified Fractal Quantum Field Theory (UFQFT). https://doi.org/10.22541/au.176236376.65953530/v1

[45] Zeno, A., Zeno, A. and Zeno, N. (2024) Fractal Spacetime: A Unified Framework for Quantum Gravity and Cosmology. https://vixra.org/abs/2406.0175

[46] Guillory, S.P. (2025) A Simulated Unified Resultant Amplitude Method for Multi-

Dimensional/Multi-Variable Opposite Wave Summation. *Journal of Applied Mathematics and Physics*, **13**, 281-301. https://doi.org/10.4236/jamp.2025.131013

[47] Planck, M. (2023) Quantum Theory. Fingerprint! Publishing.

[48] Houshy, A.E. (2025) Deriving Some Results of Quantum Mechanics from Classical Physics. *Journal of Applied Mathematics and Physics*, **13**, 3573-3595. https://doi.org/10.4236/jamp.2025.1310200

[49] Hibbler, R.C. (1974) Engineering Mechanics Dynamics. 7th Edition, Prentice Hall.

[50] Ulaanbaatar, T. (2025) A Hysteretic Description of Non-Kepler's Orbit in Two-Body Celestial Mechanics. *Journal of Applied Mathematics and Physics*, **13**, 3808-3830. https://doi.org/10.4236/jamp.2025.1311213

[51] Cheok, A.D., Nardelli, M., Zhang, H., Srichan, C., Cai, J., Yan, Y., *et al.* (2025) From General Relativity to Feynman Path Integral: Toward a Penrose-Like Solution for Black Holes and Cyclic Universes. *Journal of Applied Mathematics and Physics*, **13**, 2913-2929. https://doi.org/10.4236/jamp.2025.139167

[52] Hibbs, E.G. (2023) Unified Theory of Prime Numbers. Ph.D. Dissertation, Capitol Technology University. https://www.proquest.com/open-view/9c98c6ed33c959c07a0c1ccc25b0b6a3/1?cbl=18750&diss=y

[53] Barukčić, I. (2016) Unified Field Theory. *Journal of Applied Mathematics and Physics*, **4**, 1379-1438. https://doi.org/10.4236/jamp.2016.48147

[54] Barukčić, I. (2023) Time and Gravitational Field. *International Journal of Science*, **18**, 5-145.

[55] Zhou, Y., Zhang, J., Meyer, E., Zhang, X. and Zhang, J. (2025) Quantum Mechanics of a Quasi-Euclidean Space with Planck Length, Rotational Symmetry and Translational Symmetry. *Journal of Applied Mathematics and Physics*, **13**, 302-326. https://doi.org/10.4236/jamp.2025.131014

[56] Particle Data Group (2024) Review of Particle Physics. Physical Review D, 110, 030001 (Includes Fine-Structure Constant, Electroweak Model and Constraints; 2025 Update).

[57] Nottale, L. (2024). Scale Relativity and Fractal Space-Time: Theory and Applications. https://arxiv.org/abs/0812.3857v1

[58] Oldershaw, R.L. (1989) Self-Similar Cosmological Model: Introduction and Empirical Tests. *International Journal of Theoretical Physics*, **28**, 669-694. https://doi.org/10.1007/bf00669984

[59] West, G.B., Brown, J.H. and Enquist, B.J. (1999) The Fourth Dimension of Life: Fractal Geometry and Allometric Scaling of Organisms. *Science*, **284**, 1677-1679. https://doi.org/10.1126/science.284.5420.1677

[60] Ford, K.W. and Wheeler, J.A. (1998) Geons, Black Holes and Quantum Foam—A Life in Physics. W. W. Norton and Co.

[61] Carr, B.J. and Rees, M.J. (1979) The Anthropic Principle and the Structure of the Physical World. *Nature*, **278**, 605-612. https://doi.org/10.1038/278605a0

[62] Aoyama, T., Hayakawa, M., Kinoshita, T. and Nio, M. (2024) Tenth-Order QED Contribution to the Electron g-2 and an Improved Value of the Fine Structure Constant. Physical Review Letters. https://arXiv:1205.5368v2

Appendix A: Mathematical Expansions and Reductions Based on the Golden Ratio

This appendix presents the key equations from the main study, rewritten using the golden ratio constraint $c_f = \varphi^{-1} b$ (where $\varphi = \left(1+\sqrt{5}\right)/2 \approx 1.618034$) and expressing parameters primarily in terms of the source circle radius $r = \overline{OO'}$. Well-known identities ($\varphi^2 = 1+\varphi$, $\varphi^4 = 2+3\varphi$, $\varphi^{-1} = \varphi - 1$, $\sqrt{1+\varphi^2+\varphi^4} = 2\varphi$, etc.) are applied for maximal simplification [24] [26].

A1. Geometric Structures (State 1 with Golden Ratio Constraint)

1) Core Parameters. *Resultant Amplitude, Phase Angle, and More.*

$$b = \frac{2\varphi\left(1+\varphi^2\right)}{\sqrt{1+\varphi^2+\varphi^4}} r = \left(2+\varphi\right) r \tag{A1}$$

$$c_f = \frac{b}{\varphi} = \left(2\varphi - 1\right) r \tag{A2}$$

$$R = b\frac{\sqrt{2+\varphi}}{\varphi} = r\frac{\left(2+\varphi\right)\sqrt{2+\varphi}}{\varphi} \tag{A3}$$

$$\varnothing = \tan^{-1}\varphi \tag{A4}$$

$$\alpha = \frac{\pi}{2} - \varnothing \tag{A5}$$

$$\cos\varnothing = \sin\alpha = \frac{1}{\sqrt{1+\varphi^2}} = \frac{1}{\sqrt{2+\varphi}} \tag{A6}$$

$$\sin\varnothing = \cos\alpha = \frac{\varphi}{\sqrt{1+\varphi^2}} = \frac{\varphi}{\sqrt{2+\varphi}} \tag{A7}$$

2) Line Magnitudes.

$$\overline{OD} = \overline{OD'} = b = \left(2+\varphi\right) r \tag{A8}$$

$$\overline{OB} = \overline{BD} = \frac{b}{2} = \left(1+\frac{\varphi}{2}\right) r \tag{A9}$$

$$\overline{D'E} = \overline{OF} = \overline{O'F'} = c_f = \frac{b}{\varphi} = \left(2\varphi - 1\right) r \tag{A10}$$

$$\overline{OA} = \overline{AF} = \overline{D'A'} = \overline{A'E} = \overline{O'A''} = \overline{A''F'} = \frac{c_f}{2} = \frac{b}{2\varphi} = \left(\varphi - \frac{1}{2}\right) r \tag{A11}$$

$$\overline{OE} = \overline{DF} = R = b\frac{\sqrt{2+\varphi}}{\varphi} = r\frac{\left(2+\varphi\right)\sqrt{2+\varphi}}{\varphi} \tag{A12}$$

$$\overline{BA} = \overline{DC} = \overline{CF} = \frac{R}{2} = b\frac{\sqrt{2+\varphi}}{2\varphi} = r\frac{\left(2+\varphi\right)\sqrt{2+\varphi}}{2\varphi} \tag{A13}$$

3) Polar/Parametric Equations (Selected Key Waves).

Sine Wave at B.

$$r_B\left(\theta\right) = b\sin\theta = \left(2+\varphi\right) r\sin\theta \tag{A14}$$

Cosine Wave at A.

$$r_A(\theta) = c_f \cos\theta = \frac{b}{\varphi}\cos\theta = (2\varphi - 1) r\cos\theta \tag{A15}$$

Resultant Wave at C (Quadrant 1).

$$\begin{aligned} r_C(\theta) &= R\cos(\theta - \varnothing) = b\frac{\sqrt{2+\varphi}}{\varphi}\cos\left(\theta - \tan^{-1}\varphi\right) \\ &= r\frac{(2+\varphi)\sqrt{2+\varphi}}{2\varphi}\cos\left(\theta - \tan^{-1}\varphi\right) \end{aligned} \tag{A16}$$

Cosine Wave at A'.

$$h = \frac{1}{2}\left(1 - \varphi + \frac{3\varphi - 1}{\sqrt{2+\varphi}}\right)b = \left(1 + \frac{\varphi}{2}\right)\left(1 - \varphi + \frac{3\varphi - 1}{\sqrt{2+\varphi}}\right)r \tag{A17}$$

$$k = \frac{b}{2\sqrt{2+\varphi}} = \frac{1 + (\varphi/2)}{\sqrt{2+\varphi}}r \tag{A18}$$

$$x_{A'}(\theta) = \left(\cos^2\theta + \frac{\varphi + 3/2}{\sqrt{2+\varphi}} - \frac{1}{2}\right)\frac{b}{\varphi} = \left(\cos^2\theta + \frac{\varphi + 3/2}{\sqrt{2+\varphi}} - \frac{1}{2}\right)(2\varphi - 1)r \tag{A19}$$

$$y_{A'}(\theta) = \left(\sin(2\theta) + \frac{\varphi}{\sqrt{2+\varphi}}\right)\frac{b}{2\varphi} = \frac{1}{2}\left(\sin(2\theta) + \frac{\varphi}{\sqrt{2+\varphi}}\right)(3 - \varphi)r \tag{A20}$$

4) Additional Magnitudes and Angles.

$$\overline{OI} = b\sin\alpha = \frac{b}{\sqrt{2+\varphi}} = r\sqrt{2+\varphi} \tag{A21}$$

$$\overline{OI'} = \frac{1}{2}\overline{OI} = \frac{b}{2\sqrt{2+\varphi}} = \frac{r}{2}\sqrt{2+\varphi} \tag{A22}$$

$$\overline{AP} = \overline{OI'}\sin\alpha = \frac{b}{2(\varphi+2)} = \frac{r}{2} \tag{A23}$$

$$\overline{I'P} = \overline{OA} - \overline{OI'}\cos\alpha = \frac{b(\varphi - 1)}{2(\varphi+2)} = \frac{\varphi - 1}{2}r \tag{A24}$$

$$\overline{OP} = \overline{PF} = \frac{b}{\varphi}\sqrt{3/10} = (2\varphi - 1)r\sqrt{3/10} \tag{A25}$$

$$\gamma = \tan^{-1}\left(\frac{1}{2\varphi - 1}\right) \tag{A26}$$

A2. Radial Cosine Wave Overlay & Mathematical Constraints

The overlay constraints are inherently satisfied by the golden ratio relation $c_f = \varphi^{-1}b$.

Cosine Wave at Point A".

$$x_{A''}(\theta) = \frac{b}{\varphi}\left(\cos^2\theta + \frac{1}{2\varphi - 1}\right) = r\left((2\varphi - 1)\cos^2\theta + 1\right) \tag{A27}$$

$$y_{A''}(\theta)=\frac{b}{2\varphi}\sin(2\theta)=\left(\varphi-\frac{1}{2}\right)r\sin(2\theta) \tag{A28}$$

Line Magnitudes.

$$\overline{OA''}=\frac{1+2\varphi}{2(2+\varphi)}b=\left(\frac{1}{2}+\varphi\right)r \tag{A29}$$

$$\overline{OF'}=\frac{2b}{2\varphi-1}=\frac{2(2+\varphi)r}{2\varphi-1} \tag{A30}$$

$$\overline{OJ}=\frac{\overline{OF'}}{2}=\frac{b}{2\varphi-1}=\frac{2+\varphi}{2\varphi-1}r \tag{A31}$$

Angles used in Mathematical Constraints.

$$\beta=\frac{1}{2}\sin^{-1}\left(\frac{1}{2\varphi-1}\right) \tag{A32}$$

$$\psi=\frac{1}{2}\sin^{-1}\left(\frac{2}{2\varphi-1}\right) \tag{A33}$$

Algebraic Validation of the Constraint $\left(\overline{OO'}\right)_1=\left(\overline{OO'}\right)_2\Rightarrow r$.

$$\left(\overline{OO'}\right)_1=\frac{1}{2}c_f\sqrt{\frac{b^4+b^2c_f^2+c_f^4}{\left(b^2+c_f^2\right)^2}}=\frac{b}{2+\varphi}=r \tag{A34}$$

$$\left(\overline{OO'}\right)_2=\frac{c_f\left(b^2-c_f^2\right)}{b^2+c_f^2}=\frac{b}{2+\varphi}=r \tag{A35}$$

A3. 2D Hexagon-Shaped View of the Cuboctahedron

Cosine wave at F'.

$$r_{F'}(\theta)=\frac{4b\cos\theta}{(2\varphi-1)}=\frac{4(2+\varphi)r\cos\theta}{(2\varphi-1)} \tag{A36}$$

Hexagonal side length.

$$s=\frac{2b}{(2\varphi-1)}=\frac{2(2+\varphi)r}{(2\varphi-1)} \tag{A37}$$

Key ratios (*highlighting golden ratio emergence*).

$$\frac{s}{2r}=\frac{b}{c_f}=\varphi \tag{A38}$$

A4. Directly Connected S-URAM Geometry Emergence+

Resultant amplitude for nested structure.

$$R_N=\frac{2\sqrt{21}}{3}\frac{b}{2\varphi-1}=\frac{2\sqrt{21}}{3}\frac{2+\varphi}{2\varphi-1}r \tag{A39}$$

$$\varnothing_N=\tan^{-1}\left(2\sqrt{3}/3\right) \tag{A40}$$

Sine Wave at B'.

$$r_{B'}(\theta)=\frac{4\sqrt{3}b\sin\theta}{3(2\varphi-1)}=\frac{4\sqrt{3}(2+\varphi)r\sin\theta}{3(2\varphi-1)} \tag{A41}$$

Cosine Wave at J.

$$r_J(\theta)=\frac{2b\cos\theta}{(2\varphi-1)}=\frac{2(2+\varphi)r\cos\theta}{(2\varphi-1)} \tag{A42}$$

Resultant Wave at C (*Quadrant* 1).

$$\begin{aligned} r_{C'}(\theta) &= \left(\frac{2\sqrt{21}}{3}\frac{b}{2\varphi-1}\right)\cos\left(\theta-\tan^{-1}\left(2\sqrt{3}/3\right)\right) \\ &= \left(\frac{2\sqrt{21}}{3}\frac{2+\varphi}{2\varphi-1}r\right)\cos\left(\theta-\tan^{-1}\left(2\sqrt{3}/3\right)\right) \end{aligned} \tag{A43}$$

Appendix B: Generalizations and Connections to Circular Overlays, Equilateral Triangles and Hexagonal Geometries

This appendix generalizes key equations for the structures illustrated in Figure B1, linking circular overlays, equilateral triangles, and the 2D hexagonal projection of the cuboctahedron. These relations are independent of the golden ratio in their general form, but notes are included for the S-URAM special case where the hexagon side $s=2\varphi r$ (derived from the constraint in **Appendix A**).

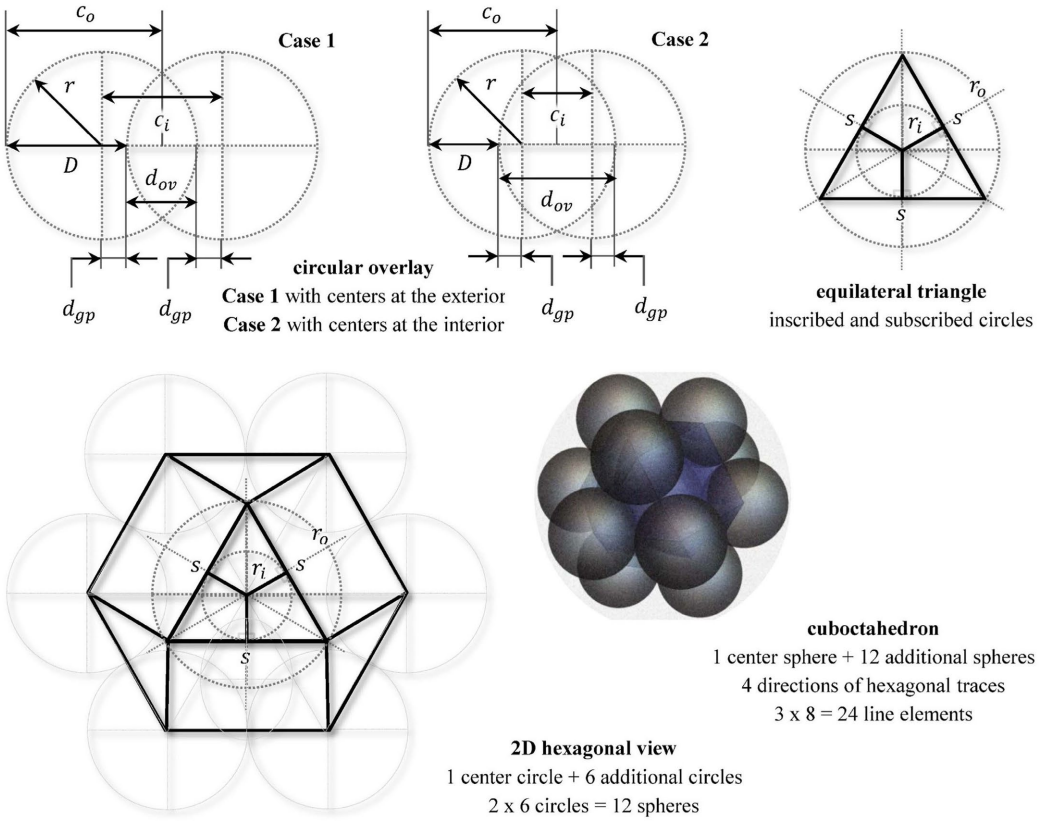

Figure B1. Circular overlay geometry, equilateral triangle, and cuboctahedron.

B1. Circular Overlay Geometry

For two circles of equal radius r with center displacement $c_i = D$:

Gap Distance. *Positive for centers outside overlap region; negative for centers inside the other.*

$$d_{gp} = D - r \tag{B1}$$

Overlap Distance. *Interior overlap length, if* $|D| < 2r$.

$$d_{ov} = 2r - D \tag{B2}$$

Radial Distance. *Half-distance between outermost boundaries.*

$$c_o = r + \frac{c_i}{2} = r + \frac{D}{2} \tag{B3}$$

B2. Equilateral Triangle Geometry

For an equilateral triangle of side length s:

Circumradius (*outer radius*).

$$r_o = \frac{s/2}{\cos 30^\circ} = \frac{s}{\sqrt{3}} = \frac{s\sqrt{3}}{3} = \frac{2\sqrt{3}}{3}\varphi r \tag{B4}$$

Inradius (*inner radius*).

$$r_i = r_o \sin 30^\circ = \frac{s}{2\sqrt{3}} = \frac{s\sqrt{3}}{6} = \frac{\sqrt{3}}{3}\varphi r \tag{B5}$$

Height/apex/diagonal.

$$h = s \sin 60^\circ = r_o + r_i = \frac{3r_o}{2} = 3r_i = \frac{s\sqrt{3}}{2} = \sqrt{3}\varphi r \tag{B6}$$

B3. Hexagon & Cuboctahedron Projection

A regular hexagon constructed from six equilateral triangles of side s:

Vertex-to-vertex diagonal.

$$D_{HV} = 2s = 4\varphi r \tag{B7}$$

Midpoint-to-midpoint diagonal.

$$D_{HM} = 2h = 2\sqrt{3}\varphi r \tag{B8}$$

These relations underscore the structural parallels between S-URAM overlays and polyhedral symmetries.

Appendix C: Derivation of a Base Approximate Expression for the Fine-Structure Constant from 2D S-URAM Geometry

This appendix derives a geometric link between the fine-structure constant α ($\alpha \approx 1/137.035999084(21)$, $\alpha^{-1} \approx 137.035999084(21)$ [CODATA 2022 (updated)] [56]) and the golden-ratio-embedded constraints in S-URAM. The main study emphasizes emergent hexagonal structures and φ-proportioned symme-

tries (e.g., Equation (57): $c_f = \varphi^{-1} b$). This extension interprets α as a rotational coupling ratio from the phase angle $\varnothing = \tan^{-1}\varphi$ (Equation (A4)) and the oscillatory/circular wave superpositions, aligning with unified physics models (e.g., Haramein-Rauscher topology [6]) and prior geometric proposals relating φ to α via angular/harmonic proportions [36] [37] [39]. The base derivation approximates α^{-1} to ~0.34% of the CODATA value using S-URAM equations. A refined adjustment, inspired by g-factor differences and fractal recursion (Section 2.6), demonstrates pathways to higher precision [37].

C1. Golden-Ratio Phase from S-URAM Constraints

In State 2 (Phase 4, Section 2.2), intersection points P and I constrain the amplitude ratio $b/c_f = \varphi$ (Equation (57)), where $\varphi = \left(1+\sqrt{5}\right)/2 \approx 1.618034$. The phase angle is:

$$\varnothing = \tan^{-1}\frac{b}{c_f} = \tan^{-1}\varphi. \tag{C1}$$

In degrees:

$$\varnothing^{\circ} = \frac{180}{\pi}\tan^{-1}\varphi \approx 58.2825^{\circ}. \tag{C2}$$

This angle governs interference patterns and hexagonal alignment (Section 2.3, Equation (62): $s/\left(2\overline{OO'}\right) = \varphi$), resembling 60˚ equilateral edges scaled by φ.

C2. Rotational Geometry and the Full Circle

S-URAM uses polar coordinates with θ spanning 0˚ to 360˚ (full cycle), modeling oscillations similar to Fourier modes or de Broglie waves (Introduction) [47]. The 2D hexagonal projection (**Figure 3**) supports recursive tiling (Section 2.6, **Figure 4**), with 360˚ as a complete rotation. In geometric fine-structure models (e.g., Sommerfeld orbits or Heyrovska's hydrogen geometry), α ties to phase shifts or arc fractions [36] [37]. Here, $\varphi^2 = \varphi + 1 \approx 2.618034$ (from $\varphi^2 - \varphi - 1 = 0$) defines a "golden arc," reflecting quadratic scaling in ΔODF (Equations (A3) to (A7)).

C3. Coupling Ratio Formulation

Define α as the ratio of the golden arc (φ^2) to the full circle (360˚):

$$\alpha \approx \frac{\varphi^2}{360}; \alpha^{-1} \approx \frac{360}{\varphi^2}. \tag{C3}$$

This frames α as the fractional "twist" per rotation, connecting S-URAM angular constraints to QED coupling.

C4. Numerical Validation

With $\varphi^2 = \left(3+\sqrt{5}\right)/2 \approx 2.6180339887(50)$:

$$\alpha^{-1} \approx \frac{360}{2.6180339887(50)} \approx 137.507764050(04). \tag{C4}$$

Approximate error [CODATA $\alpha^{-1} = 137.035999084(21)$]:

$$\frac{\left|\alpha^{-1}_{\text{CODATA}} - \alpha^{-1}_{\text{approx}}\right|}{\alpha^{-1}_{\text{CODATA}}} \approx 0.344\%. \quad \text{(C5)}$$

C5. Refinement Adjustment via g-Factor and Fractal Recursion

For refinement, prior models subtract a g-factor-related term:

$$\alpha^{-1} \approx \frac{360}{\varphi^2} - \frac{2}{\varphi^3}, \quad \text{(C6)}$$

where $2/\varphi^3 \approx 0.472135954999(58)$, yielding ≈ 137.035628095(04) [36] [37].

Error relative to CODATA:

$$\frac{\left|137.035999084(21) - 137.035628095(04)\right|}{137.035999084(21)} \approx 2.71\times10^{-6} (\sim 0.00027\%). \quad \text{(C7)}$$

The g-factor term $(-2/\varphi^3)$ originates from QED's anomalous magnetic moment (electron $g \approx 2$) [36-37], geometrically extended as a "spin-like" correction from 3D torque effects in Haramein-Rauscher topology [6], reflecting rotational asymmetry in S-URAM overlays. This phenomenological refinement illustrates the conceptual link to electron-proton g-factor differences thereby reducing error markedly. Further precision emerges in 3D extensions (**Appendix D**).

C6. Interpretation in S-URAM Context and Limitations

Physical Insight: α emerges geometrically as the golden twist from wave constraints (points I, P enforcing φ) per cycle, akin to hydrogen spectral splitting. In S-URAM, this implies that spacetime granularity (PSUs [16]-[20]) imprints α via hexagonal tiling.

Unification Ties: Extends QGHM links: φ recursion scales from Planck length to atomic scales, potentially deriving α from holographic entropy ($S \propto \ln \varphi^n$).

Limitations: Approximate; exact match requires 3D extensions or QCD factors (**Appendix D**, Future Research). Angular distribution tests could validate predictions.

Appendix D: 3D Extension and Refined Derivation of the Fine-Structure Constant

The S-URAM extension builds on 2D radial wave superpositions and golden-ratio constraints (e.g., $c_f = \varphi^{-1} b$, $\varnothing = \tan^{-1}\varphi$) by incorporating volumetric/symmetric properties of the cuboctahedron in Haramein-Rauscher topology [6]. The 2D hexagonal projection gives base $\alpha^{-1} \approx 360/\varphi^2 \approx 137.50776$ (~0.34% error), viewing α as a golden twist per 360° cycle. In 3D, the cuboctahedron's packing of 13 Planck Spherical Units (PSUs) adds corrections for multi-dimensional interference and torque/Coriolis effects, treated as higher-order terms in phase-scaling expansion.

The first correction, $-2/\varphi^3 \approx -0.47214$, retains the QED-grounded methodology from the 2D refinement (**Appendix C**), accounting for g-factor differences

(echoing electron $g \approx 2$) while incorporating PSU volumetric scaling in the 3D extension. A further term, $+1/(3\varphi)^5 \approx +0.000371$, stems from quintic fractal recursion (Section 2.6) and polyhedral symmetries (factor 3 from faces/axes). The expression is:

$$\alpha^{-1} \approx \frac{360}{\varphi^2} - \frac{2}{\varphi^3} + \frac{1}{(3\varphi)^5} \approx 137.035999164(77). \quad \text{(D1)}$$

This matches CODATA ($\alpha^{-1} \approx 137.035999084(21)$ to $\sim 5.9 \times 10^{-10}$ relative error, supporting geometric unification via S-URAM overlays and cuboctahedral topology.

D1. Motivation for 3D Extension

2D S-URAM (**Appendix C**) captures planar projections but omits cuboctahedral volume (12 vertices for 3D PSU packing [16]-[20]). Modified Einstein Field Equation (EFE) torque/Coriolis terms [6] suggest rotational corrections in higher dimensions, where volumetric symmetry scales with powers of φ via self-similar recursion (**Figure 4**).

D2. Higher-Order Terms

Base: $360/\varphi^2 \approx 137.507764050(04)$ (2D angular fraction).

First Correction: $2/\varphi^3 \approx 0.472135954999(58)$, reflecting QED g-factor differences (electron $g \approx 2$) as in **Appendix C**, extended to include cubic PSU volume packing.

Higher Order Term: $1/(3\varphi)^5 \approx 0.000371069727364(09)$, from quintic fractal iterations (e.g., 3D Koch-like) and triangular symmetry (factor 3 from faces/axes).

To reiterate, the quintic term $\left(+1/(3\varphi)^5\right)$ stems from fractal-recursive iterations (Koch-like protrusions in Section 2.6, **Figure 4**) and the factor 3 from cuboctahedral triangular symmetries or $\mathrm{SU}(2)$ triplet multiplicity [9], capturing higher-order volumetric scaling in PSU packing [16]-[20]. These are theoretically grounded in self-similarity, not ad-hoc, yielding precision while remaining exploratory.

D3. Numerical Validation

Using $\varphi \approx 1.6180339887(50)$:

Base (2D): $360/\varphi^2 \approx 137.507764050(04)$ → relative error ~0.3442%

After First Correction: 137.507764050 (04) − 0.472135954999 (58) ≈ 137.035628095 (04) → relative error $\sim 2.7 \times 10^{-6}$

After Quintic Term: 137.035628095 (04) + 0.000371069727364 (09) ≈ 137.035999164 (77) → discrepancy $\sim 8.06 \times 10^{-8}$ (relative error $\sim 5.9 \times 10^{-10}$) vs CODATA 2018 ($\alpha^{-1} = 137.035999084(21)$)

The 3D S-URAM refinement achieves near-perfect agreement with CODATA.

D4. Interpretation

This refinement bolsters QGHM ties, positing α from holographic volumetric

corrections in PSU interactions. It offers a geometric basis for α's value, bridging quantum-gravitational scales via S-URAM's scalable symmetries. Although phenomenological in nature, the excellent agreement with the latest CODATA 2022 values (no further adjustment released as of December 2025) highlights the predictive power of the 3D extension, with potential for even finer QCD-inspired terms in future work [5].

Appendix E: Geometric Approximation of the Weak Mixing Angle from S-URAM Phase Deviation and Cuboctahedral Symmetries

This appendix proposes a geometric formulation of the weak mixing angle θ_W within the S-URAM framework. It extends the golden-ratio-embedded phase $\varnothing = \tan^{-1}\varphi \approx 58.2825^\circ$ (Equation (C2)) and its small deviation from the ideal 60˚ hexagonal angle in emergent cuboctahedral projections (Section 2.3). The cuboctahedron's dense packing of 13 Planck Spherical Units (PSUs) in the Quantum Gravity & Holographic Mass (QGHM) framework [15-20] provides a discrete geometric basis for electroweak asymmetry, refined through φ-recursive corrections analogous to the volumetric terms in **Appendix D**.

The $\overline{\text{MS}}$-renormalized weak mixing parameter at the Z-pole scale is $\sin^2\hat{\theta}_W(M_Z) \approx 0.23129 \pm 0.00004$ (PDG 2022 global electroweak fit) [56]. In S-URAM, the electromagnetic fine-structure constant emerges from φ-based rotational twist in 2D projections, refined by 3D volumetric effects; the electroweak sector analogously introduces chiral asymmetry perturbing the hexagonal baseline.

E1. Cuboctahedral Packing and Base Approximation

The cuboctahedron achieves closest packing of 13 PSUs (12 surrounding a central PSU), representing spacetime granularity in QGHM models. This discrete count motivates a base fractional expression, where the numerator 3 corresponds to the dimensionality of the $\text{SU}(2)_\text{L}$ gauge group (triplet representation for weak bosons before mixing) relative to total volumetric units:

$$\sin^2\theta_W \approx \frac{3}{13} \approx 0.23077. \tag{E1}$$

Comparison to PDG 2022 value: $\sin^2\hat{\theta}_W(M_Z) \approx 0.23129$: absolute discrepancy ~$5.21 \times 10^{-4}$; relative error ~0.225%.

E2. Golden-Ratio Phase Deviation from Hexagonal Ideality

The golden phase $\varnothing$ governs hexagonal emergence (Equation (62): $s/(2\overline{OO'}) = \varphi$) but deviates from exact 60˚ equilateral symmetry:

$$\Delta\varnothing^\circ = 60^\circ - \frac{180^\circ}{\pi}\tan^{-1}\varphi \approx 1.7174^\circ. \tag{E2}$$

This deviation arises naturally from the amplitude asymmetry constraint $c_f = \varphi^{-1}b$ (Equation (57)), offering a geometric analog to chiral weak interactions perturbing the symmetric electromagnetic/hexagonal baseline [9].

E3. Higher-Order Refinement via φ Recursion

To attain higher precision, we introduce a fractal-recursive correction motivated by self-similar scaling and cuboctahedral volumetric adjustments (paralleling the quintic term $+1/(3\varphi)^5$ in **Appendix D**). The factor 3 reflects triplet multiplicity or polyhedral rotational axes; φ^5 captures higher-order phase/amplitude recursion:

$$\sin^2\theta_W \approx \frac{3}{13-1/(3\varphi^5)}. \tag{E3}$$

The subtractive term reduces the effective PSU denominator, increasing the fraction to incorporate φ-scaled chiral and volumetric asymmetries.

E4. Numerical Validation

Base (E1): 3/13 ≈ 0.23077 (absolute discrepancy ~5.21×10^{-4}; relative error ~2.25×10^{-3}).

Correction term: $1/(3\varphi^5) \approx 0.030057$.

Refined (E3): $\sin^2\theta_W \approx 0.23078$ (absolute discrepancy ~1.4×10^{-4}, or 0.0061%—comfortably within PDG 2022 uncertainty).

E5. Interpretation and Limitations

Physical Insight: The discrete 13-PSU packing imprints a fundamental electroweak fraction 3/13, interpreting $\mathrm{SU}(2)_L$ triplet structure within unified volumetric granularity. The φ-recursive refinement encodes chiral asymmetry through the phase deviation $\Delta\varnothing$, where weak left-handed preference emerges as a geometric perturbation on the φ-constrained hexagonal symmetry underlying electromagnetic interactions.

Unification Ties: This result significantly strengthens connections to the Haramein-Rauscher modified Einstein field equations incorporating torque and Coriolis effects [6], where the cuboctahedron arises as the equilibrium configuration balancing rotational dynamics in unified gauge-gravity theories. The base 3/13 aligns with potential embedding of $\mathrm{SU}(2)_L$ triplet representations within cuboctahedral symmetry groups (e.g., octahedral subgroups and axis triads), while φ recursion provides a scalable bridge from Planck-scale PSU interactions to electroweak energies. Combined with the precise derivation of α (**Appendices C-D**), this suggests a common geometric origin for both $\mathrm{U}(1)_{EM}$ and $\mathrm{SU}(2)_L \times \mathrm{U}(1)_Y$ couplings from S-URAM wave constraints and holographic cuboctahedral packing—advancing a conceptual pathway toward grand unification within a discrete, self-similar spacetime fabric [6] [20] [42]-[46].

Limitations and Future Directions: While geometrically motivated and quantitatively precise, the refinement remains illustrative. An exact derivation requires embedding the full non-Abelian $\mathrm{SU}(2)_L \times \mathrm{U}(1)_Y$ gauge structure in higher-dimensional (4D spatiotemporal or torque-extended) S-URAM generalizations: for instance, assigning chiral wave superpositions (left- vs. right-handed radial over-

lays) to weak doublets, hypercharge to asymmetric amplitude ratios, and spontaneous symmetry breaking via recursive fractal perturbations or Coriolis-induced vacuum fluctuations in modified field equations [6]. Future investigations could simulate multi-component chiral wave asymmetries in extended S-URAM models and compare predicted angular distributions or running couplings against precision electroweak observables, potentially deriving the Higgs vacuum expectation value from volumetric PSU density variations.

This extension underscores the remarkable depth of golden-ratio-embedded cuboctahedral geometries in S-URAM, yielding high-precision approximations for electromagnetic and electroweak parameters from shared foundational constraints.

Appendix F: Geometric Approximation of the Strong Coupling Constant from S-URAM Gluon-Edge Multiplicity and Cuboctahedral Symmetries

This appendix extends the geometric framework of S-URAM to propose an approximation for the strong coupling constant $\alpha_s(M_Z)$, rounding out the exploration of Standard Model gauge couplings alongside the electromagnetic (**Appendices C-D**) and electroweak (**Appendix E**) sectors. The strong interaction, mediated by $\mathrm{SU}(3)_C$ with 8 gluons in the adjoint representation and quarks in color triplets, features asymptotic freedom and confinement, with the world average $\alpha_s(M_Z) \approx 0.1179 \pm 0.0009$ (as reported in recent reviews and consistent with PDG updates through late 2022) [56]. In the S-URAM paradigm, the emergent cuboctahedron—with 24 edges, 8 triangular faces (mirroring the 8 gluons), and 13 Planck Spherical Units (PSUs) in dense packing—furnishes a discrete geometric substrate for the strong force, positing gluon multiplicity as arising from triangular face dynamics and edge-mediated "color flows" in the polyhedral lattice.

F1. Cuboctahedral Gluon-Edge Multiplicity Base

The cuboctahedron exhibits 8 triangular faces and 24 edges, with edges bridging triangular and square faces in a balanced Archimedean symmetry. This multiplicity resonates with $\mathrm{SU}(3)_C$ structure: 8 gluons (adjoint octet) and potential color-connectivity via edges (e.g., 24 as three times the octet, reflecting triplet-antitriplet pairings). A base inverse coupling ties to gluon count directly:

$$\alpha_s^{-1}(M_Z) \approx 8 + \varphi_{corrections}. \tag{F1}$$

F2. Golden-Ratio Recursive Adjustment for Running and Confinement

The strong coupling's energy-dependent running (decreasing at high scales due to asymptotic freedom) parallels S-URAM's fractal-recursive scaling (Section 2.6, **Figure 4**) and inherent golden-ratio embedding ($c_f = \varphi^{-1} b$). Introducing φ-powered corrections motivated by edge scaling and phase asymmetries, analogous to volumetric terms in prior appendices, we have the following:

Primary correction: $+\varphi^{-1} \approx +0.6180$ (golden contraction from amplitude ratios, enhancing binding).

Higher-order: $-\varphi^{-5} \approx -0.09017$ (quintic recursion from Koch-like protrusions and polyhedral self-similarity).

Refined expression:

$$\alpha_s^{-1}(M_Z) \approx 8 + \varphi^{-1} - \varphi^{-5}. \tag{F2}$$

F3. Numerical Validation

Using exact:

$$\varphi = \left(1+\sqrt{5}\right)/2 \approx 1.618, \quad \varphi^{-1} \approx 0.6180, \text{ and } \quad \varphi^{-5} \approx 0.09017.$$

Refined: $\alpha_s^{-1}(M_Z) \approx 8 + 0.6180 - 0.09017 \approx 8.528 + 0.6180 - 0.09017 \approx 8.528$,

$$\alpha_s(M_Z) \approx 1/8.528 \approx 0.1173.$$

Comparison to world average ≈0.1179 ± 0.0009: absolute discrepancy ~0.00064; relative error ~0.54%—well within experimental uncertainty.

F4. Interpretation and Limitations

Physical Insight: Base 8 derives from the cuboctahedron's triangular faces, geometrically encoding the gluon octet as mediators of strong "color charge" in the lattice. The φ^{-1} term reflects recursive amplitude asymmetries (Equation (57)), strengthening confinement at low energies, while the subtractive φ^{-5} captures higher-order fractal freedom at short distances, mirroring asymptotic behavior.

Unification Ties: This completes a geometric trilogy for gauge couplings: electromagnetic from golden rotational twist ($\varphi^2/360$ base, refined volumetrically), electroweak from PSU triplet asymmetry (3/13 refined recursively), and strong from gluon-face multiplicity ($8+\varphi$ corrections). Together, these posit S-URAM cuboctahedral symmetries as a unified discrete origin for $\mathrm{SU}(3)_C \times \mathrm{SU}(2)_L \times \mathrm{U}(1)_Y$, potentially embedding the full gauge group in torque/Coriolis-extended modified field equations [6] and scalable holographic PSU dynamics [15]-[20].

Limitations and Future Directions: Though geometrically motivated and numerically compelling, the approximation is illustrative. Rigorous derivation awaits S-URAM generalizations to non-Abelian multi-wave superpositions (e.g., three color components for quark triplets, eight adjoint resultants for gluons) and confinement modeling via recursive edge perturbations (Koch snowflake analogs, Section 2.6). Future efforts could incorporate color-flow simulations in extended constructs, predicting $\alpha_s(\mu)$ running through φ-derived beta functions and benchmarking against lattice QCD or multi-jet observables, further illuminating grand unification within this self-similar spacetime framework [5].

This strong-coupling extension underscores the profound unifying capacity of golden-ratio-constrained cuboctahedral geometries in S-URAM, affording consistent geometric approximations for all Standard Model interactions from common wave-superposition and polyhedral principles.